REPORT DOCUMENTATION PAGE

Form Approved
OMB NO. 0704-0188

1. AGENCY USE ONLY (Leave Blank)	2. REPORT DATE 31 July 2004	3. REPORT TYPE AND DATES COVERED Final Report: 01 May 2001 - 30 April 2004

4. TITLE AND SUBTITLE
Flame Spreading and Combustion Behavior of Gun Propellants Packed in High Loading Densities

5. FUNDING NUMBERS
- DAAD19-01-1-0573

6. AUTHOR(S)
Kenneth K. Kuo and Pete Ferrara

7. PERFORMING ORGANIZATION NAME(S) AND ADDRESS(ES)
The Pennsylvania State University
Department of Mechanical and Nuclear Engineering
University Park, PA 16802

8. PERFORMING ORGANIZATION REPORT NUMBER

9. SPONSORING / MONITORING AGENCY NAME(S) AND ADDRESS(ES)
U. S. Army Research Office
P.O. Box 12211
Research Triangle Park, NC 27709-2211

10. SPONSORING / MONITORING AGENCY REPORT NUMBER
-41416-EG
01

11. SUPPLEMENTARY NOTES
The views, opinions and/or findings contained in this report are those of the author(s) and should not be construed as an official Department of the Army position, policy or decision, unless so designated by other documentation.

12 a. DISTRIBUTION / AVAILABILITY STATEMENT
Approved for public release; distribution unlimited.

12 b. DISTRIBUTION CODE

13. ABSTRACT (Maximum 200 words)
See Foreword

14. SUBJECT TERMS
JA2 propellant, Double-ended windowed strand burner, high loading density, gap width effect

15. NUMBER OF PAGES
99

16. PRICE CODE

17. SECURITY CLASSIFICATION OR REPORT	18. SECURITY CLASSIFICATION ON THIS PAGE	19. SECURITY CLASSIFICATION OF ABSTRACT	20. LIMITATION OF ABSTRACT
UNCLASSIFIED	UNCLASSIFIED	UNCLASSIFIED	UL

NSN 7540-01-280-5500

Standard Form 298 (Rev.2-89)
Prescribed by ANSI Std. 239-18
298-102

FOREWORD

The combustion process of gun propellants packed in high loading density conditions can differ significantly from those burning individually in the same pressure and temperature environment. More specifically, burn rates and flame spreading processes for a propellant charge are not only functions of pressure and initial temperature, but also a function of the loading density (or gap width between adjacent propellants). This experimental study has been conducted to investigate the influence of gap space between propellants on propellant regression rates. In the experimental setup, two opposing strands of JA2 gun propellant were burned in a double-ended windowed strand burner (DEWSB). The DEWSB consists of two identical propellant feeding systems adjoined to a center combustion chamber. To measure the gap width between the two strands, a contrasting image between the propellant strands and the background was used. To obtain a constant gap width between the opposing propellants, an image was imported into a LabVIEW control feedback loop. A series of tests was conducted for a pressure range from 0.69 to 3.45 MPa, and a gap distance range from 2 to 12 mm. Comparing regression rate data of JA2 propellant burned in the double-end configuration to that of a single strand, an increase in the regression rate of about 30% was observed for the pressure range tested. This increase occurs for a certain gap width range, which was found to be a function of pressure. The enhancement of the burn rate is caused by the geometric confinement of the flame, which applies a greater energy feedback to the burning propellant surface.

TABLE OF CONTENTS

LIST OF FIGURES

LIST OF TABLES

NOMENCLATURE

SYMBOL	DESCRIPTION	UNITS
c_p	specific heat at constant pressure	[kJ/kg-K]
D	diameter	[mm]
d_1	distance to first propellant surface	[mm]
d_2	distance to second propellant surface	[mm]
d_a	averaged on-screen gap width	[mm]
d_c	on-screen measured correction diameter	[mm]
d_{fs}	flame standoff distance	[mm]
d_{gap}	gap width between propellant strands	[mm]
d_m	LabVIEW measured gap width	[mm]
d_{m1}	measured on-screen instantaneous gap width at t_1	[mm]
d_{m2}	measured on-screen instantaneous gap width at t_2	[mm]
d_p	actual specific diameter of the propellant sample	[mm]
d_s	user specified gap width	[mm]
f_1	focal length of the plano-concave expanding lens	[mm]
f_1	focal length of the plano-convex lens	[mm]
h	height	[mm]
I_f	heat flux feedback due to radiation	[W/m^2]
L	heat of phase transition	[W/m^2]
P	pressure	[MPa]
P_{ref}	reference pressure	[MPa]
Q	heat release	[kJ/kg]
q_i	heat of chemical reactions in the solid	[W/m^2]
Q_o	heat flux feedback from flame zone to burning surface	[W/m^2]
r_b	burn rate	[mm/s or cm/s]
T	temperature	[K]
t	time	[s]

t_1	time when constant gap width starts	[s or ms]
t_2	time when constant gap width ends	[s or ms]
u	velocity	[mm/s]
V	velocity	[mm/s]
V_{base}	base-speed linear drive velocity	[mm/s]
V_{high}	high-speed linear drive velocity	[mm/s]
y_1	initial laser beam radius	[mm]
y_3	final laser beam radius	[mm]
GREEK SYMBOL	DESCRIPTION	UNITS
δ	error	
λ	thermal conductivity	[W/m-K]
θ_1	initial laser beam divergence angle	[mrad]
θ_3	final laser beam divergence angle	[mrad]
ρ	density	[g/cm^3 or kg/m^3]
SUBSCRIPTS	DESCRIPTION	UNITS
a	pre-exponential coefficient for Saint Robert's Law	
d	darkzone	
dz	darkzone	
f	flame	
g	gaseous	
ign	ignition	
L	left side	
m	pressure normalization exponent	
n	Saint Robert's Law pressure exponent	
o	initial	
p	propellant	
R	right side	
s	surface	

CHAPTER 1 Research Motivation and Objectives

1.1 Research Goals

The main propellant used in many large caliber weapons is the gun propellant JA2. Generally, it is known that increasing the propellant loading density in the cartridge can enhance the performance of a large caliber gun system. However, there are aspects of high loading density that have not been adequately studied. The gap distance between adjacent propellant grains can have a strong influence on the flame spreading phenomena as well as propellant regression rate. Due to close proximity of neighboring propellant grains, the burn rate of the propellant grains can be different from their normal burn rate when the loading density is very high. If the propellant burn rate is enhanced by the close proximity of the adjacent grains or disks during the initial phase of the ballistic cycle, the requirement for achieving high ratios (e.g. 3.0) of fast-to-slow burn rate of layered propellants is even harder to achieve.

Field and Kuo[1,2] designed a special test rig and control system consisting of a double-ended windowed strand burner. They utilized this device to conduct a preliminary study of the gap width effect of NOSOL363, a homogeneous propellant, at pressures between 0.72 and 2.3 MPa. They found that for this low-energy propellant the gap width effect is quite negligible even when the gap width was maintained at 1 mm. The burn rate correlation of opposing double strands is nearly the same as that of a single strand. They also utilized this test rig to study the burning surface behavior of the NOSOL363 propellant, and found the formation of many localized reactive centers on the propellant surface layer. The luminous flame does not seem to provide a major energy feedback to the burning surface. Thus, the gap width between adjacent burning NOSOL363 propellants does not show any significant effect on the propellant regression rate.

The main goal of this project is to experimentally investigate the effect of high loading density on the combustion behavior of the homogeneous gun propellant JA2. To complete this work, the existing test rig and control system has been upgraded with a more advanced computer controlled dual-strand feeding system for studying the JA2 propellant burning behavior. A diode-pumped solid-state laser with optics and a computer with LabVIEW and IMAQ software have been employed to obtain the instantaneous gap width image for controlling the feeding rate. Using this method, the burning rate of JA2 propellant was studied as a function of the gap width and chamber pressure. In addition, the thermal profiles of the JA2 propellant under different pressure conditions were studied.

1.2 Research Motivation

High loading density conditions permit the use of a lower energy, less vulnerable solid propellant to achieve a required muzzle velocity. These two characteristics allow the propellant sticks be bundled or disks to be pre-packed. These bundles facilitate assembly and loading in large caliber cartridges. The gap-width effect produced by high loading density conditions has not been adequately studied in the past. A better understanding of the combustion behavior under high loading density conditions is required to improve and predict the performance of the early phase behavior in the ballistic cycle.

1.3 Research Objectives

There are many benefits to studying the gap-width effect on the combustion of JA2 propellant. The specific objectives of this research are:

1. To upgrade the existing DEWSB test rig capable of maintaining a constant gap between propellant strands as they regress due to the combustion process;
2. To accurately measure the instantaneous gap width between burning propellant strands;

3. To acquire better understanding of the combustion behavior of the JA2 gun propellant under high loading density conditions, especially during the early phase of the ballistic cycle when the chamber pressure is low;
4. To determine the gap width effect on the burn rate of JA2 propellant under controlled chamber pressures;
5. To correlate the experimental data; and
6. To study the burning surface phenomena under well controlled gap width condition.

CHAPTER 2 Steady-State and Transient Burning Characteristics Of JA2 propellant

The instantaneous burning rate of a given propellant under rapidly changing pressure condition in rockets and gun systems could be significantly different from the steady-state burning rate measured in a strand burner. Under transient conditions with large amplitude pressure variations, the instantaneous regression rate cannot be determined solely by the instantaneous pressure level, largely due to the delayed time response of the thermal profile in the solid propellant. Because of the importance of the transient (also called dynamic) burning process in various propulsion systems, this topic has been studied both theoretically and experimentally by various researchers as described in two book chapters.[3,4] A review of the physical phenomena and pioneering work was given by Kuo and Coates.[5] Essentially, the transient burning phenomenon is caused by the finite time lags associated with adjustment of temperature profiles in the un-reacted solid phase and in the surface reaction zone, and the energy release rate and flame structure in the gaseous flame.

It has been observed experimentally that the transient burning effect depends on a large number of parameters, including: maximum pressurization rate, the entire history of the pressure-time curve; temperature sensitivity, pressure exponent of the propellant; exothermic heat release at the surface reaction zone, activation energy of the propellant, initial temperature of the propellant, and its thermal properties, etc.[3]

Physically, the transient burning effect is introduced during rapid pressure changes by the finite time interval required for temperature profiles inside the condensed phase, and possibly the reaction zone, to follow transient pressure variations. The faster the pressure changes, the longer the time (relative to the characteristic time of the pressure change) required for temperature

profiles to adjust themselves to the new condition. Until temperature profiles in the solid phase and the surface reaction zones are adjusted to the thermal profile corresponding to the steady-state burning at the new pressure, there is an out-of-phase blowing effect of the chemically reacting gases leaving the burning surface.

Study of dynamic burning characteristics of propellants is complicated by the difficulty of obtaining highly transient data related to phenomenon occurring in the gas phase. To bypass this difficulty, Zel′dovich suggested a way in which the heat feedback to the solid propellant immediately beneath the burning surface could be found using the steady-state experimental data, the Arrhenius burning rate law, and the relationship between the energy flux at burning surface and the energy gained from the initial temperature of the propellant to the surface temperature.[6]

Thus, following the Zel′dovich procedure to study the dynamic burning rate of a propellant, it is possible to bypass all detailed flame structure analysis by solving only the one-dimensional transient energy equation in the condensed phase, if the quasi-steady assumption of the flame is satisfied (i.e., $\tau_g << \tau_p$, $\tau_c \sim \tau_p$). Assuming that there is no subsurface heat generation, the energy equation can be written as:

$$\frac{\partial T}{\partial t} + r_b \frac{\partial T}{\partial x} - \alpha_c \frac{\partial^2 T}{\partial x^2} = 0 \qquad [-\infty \le x \le 0] \tag{2-1}$$

Initial Condition: $$T(x,0) = T_i + (T_{s,o} - T_i)\exp\left(\frac{r_b x}{\alpha_c}\right) \tag{2-2}$$

Boundary Condition 1: $$T(-\infty, t) = T_i \tag{2-3}$$

Boundary Condition 2: $$\frac{\partial T}{\partial x}(0_-, t) = \varphi_{c,s}\left[r_b(t), P(t)\right] \tag{2-4}$$

Zel′dovich Map provides the temperature gradient function from the definition.[3]

$$\varphi_{c,s}[r_b, P] = \left.\frac{\partial T}{\partial x}\right|_{\text{Burning Surface}} = \frac{r_b(T_s - T_i)}{\alpha_c} \tag{2-5}$$

JA2 is a modified double-base gun propellant used in ballistic systems. It consists of 59.50 % nitrocellulose (with 13.14 % N), 14.90 % nitroglycerin, 24.80 % diethylene glycol dinitrite (DEGDN), 0.70 % N′-methyl-N-N-diphenylurea (Akardite II, $C_{14}H_{14}N_2O$), 0.05 % magnesium oxide, and 0.05 % graphite by weight.

Some steady-state burning data and transient burning behavior of JA2 were reported by several researchers using various methods.[7,8,9,10] Some burning rate data were obtained from closed-bomb testing by the U.S. Army. However it is difficult to determine the burning surface temperature and the temperature profiles using the closed bomb method. Therefore, optical strand burner was adopted to investigate the burning rate behavior and the thermochemical properties of JA2 in the present investigation.

2.1 Experimental Approach

A high-pressure optical strand burner was utilized to conduct experiments on JA2 propellant strands. The system has a stainless steel chamber, an electric heater, and a cryogenic chiller to control the sample initial temperature at a desirable level by the heated or chilled purge gas. S-type thermocouples made of pure platinum and 10% rhodium/platinum bare wires were used for monitoring the purge gas temperature, and hence the propellant initial temperature. The chamber can withstand a maximum operating pressure of around 62 MPa. A purge gas pressurization and exhaust system is utilized with the optical chamber, in order to provide the desired pressure environment. A Setra 206 pressure transducer was used to monitor the pressure of the gas inside the chamber. The chamber is equipped with 8 rectangular side ports diametrically opposite with a viewing area of 9.5 cm x 3.2 cm. The chamber has several

diagnostic ports, through which break wire and thermocouple signals are obtained from the tested propellant strand. The signals are fed to a multi-channel data acquisition system for storage and analysis. The eight long side windows are used for optical viewing of propellant flame zones.

In strand burner tests, JA2 propellant samples of the following specifications were used. The overall sample length was 5.7 cm and the diameter was 0.635 cm. It consisted of two pieces. On one end of the larger piece, an inverted conical cup space was accurately machined, while in the smaller piece, a protruded cone with a flat top was machined to match with the cup space. At the matching interface, a fine-wire S-type thermocouple with an average thickness on the order of 2 to 5 μm was embedded in the sample at a distance of 4.45 cm from the top of the sample. The sample was coated on the lateral surface with finger nail polish to prevent the flame from spreading along the lateral surface thereby the regression takes place in a one-dimensional manner along the axis of the sample. The thermocouple was carefully installed on the platform of the truncated cone surface. Then the cup was put over it and sealed with acetone. Prior to thermocouple installation, a nichrome wire was inserted near the top surface of the propellant sample and was used for ignition during the test. Two break-wires (fuse wire) were installed at 1.27 and 3.17 cm from the top of the sample, respectively to obtain propellant burning rate in addition to visual records. During sample regression, the temperature profile in the propellant across the burning surface was measured using the embedded fine-wire thermocouple.

2.2 Task I Results and Discussion

2.2.1 Regression Rate and Temperature Sensitivity

The regression rate data were reduced, compiled, and correlated. Several correlations were established using the data for broad ranges of pressure and initial temperatures. All the burning rate data were correlated to the following expression:

$$r_b = aP^n \exp\left[\sigma_p \left(T_i - T_{i,ref}\right)\right] \tag{2-6}$$

where $T_{i,ref}$ = 298 K and temperature sensitivity (σ_p) was considered as a function of pressure according to the following expression:

$$\sigma_p = \sigma_{p,c} + \frac{b}{c_1 + c_2 P} \tag{2-7}$$

The definition of temperature sensitivity σ_p is given by Eq. (2-8)

$$\sigma_p \equiv \left.\frac{\partial \ln r_b}{\partial T_i}\right|_p \tag{2-8}$$

The parameter values obtained from the curve fitting procedure are

$a = 0.2478$ (cm/s)(MPa)$^{-n}$, $n = 0.8222$

$\sigma_{p,c} = 0.00240$ K^{-1}, $b = 0.0537$ K^{-1}, $c_1 = 17.0425$, $c_2 = 2.2108$ MPa^{-1}

The initial temperature of the samples was between -40 ^{o}C and 60 ^{o}C. It is obvious that most of the data points are near the correlation surface.

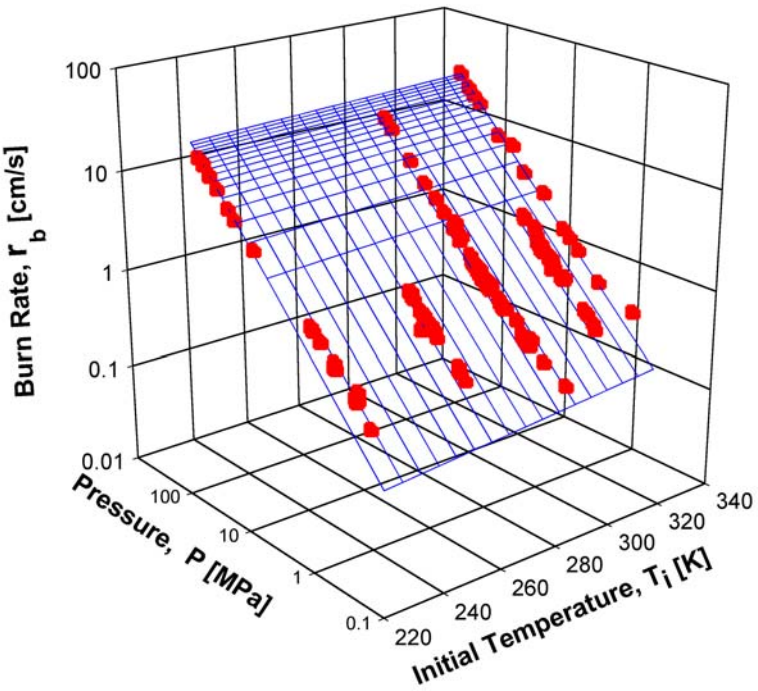

Figure 2.1 Comparison of correlated burning rate expression of JA2 propellant with the measured data, including some high-pressure data obtained earlier at PSU and U.S. Army.

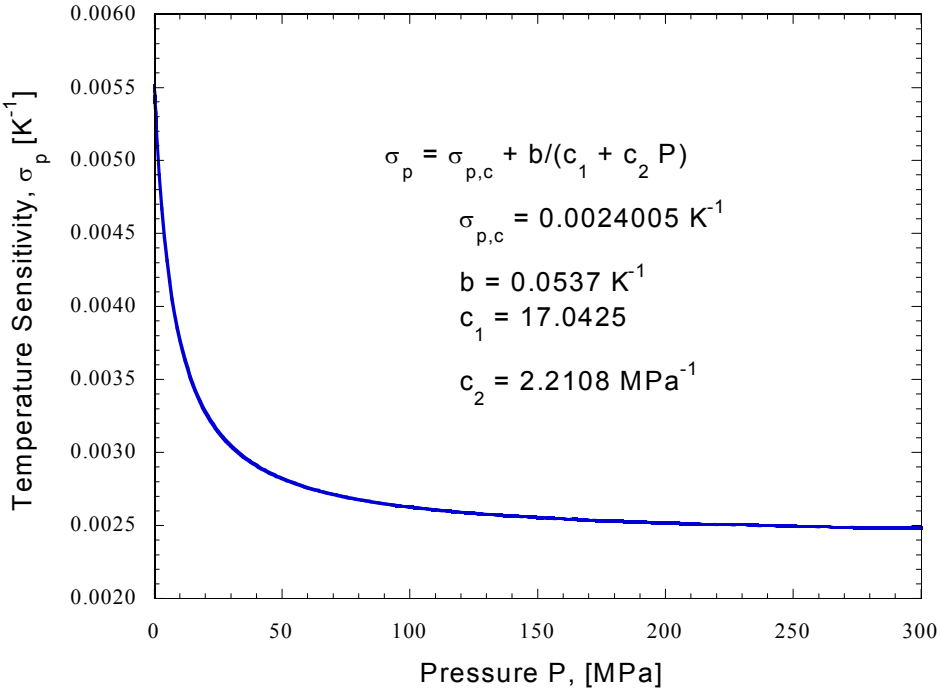

Figure 2.2 Temperature sensitivity (σ_p) of JA2 propellant as a monotonically decreasing function of pressure.

Figure 2.2 shows σ_p of JA2 propellant as a function of pressure. It is apparent from the plot that for the high-pressure range σ_p does not vary significantly. In the low-pressure range, however, temperature sensitivity falls sharply with increase of pressure.

2.2.2 Propellant Surface Temperature Determination

A micro-thermocouple trace for JA2 propellant burning at 34.6 MPa (5,000 psig) with initial temperature of 221K is shown in Figure 2.3. The surface temperature is near 750 K. Knowing the burning rate of the propellant at this pressure the horizontal axis can be transformed into distance. It is useful to note that if the thermal properties of the propellant are constant, the temperature profile should be linear on a semi-log plot.

As shown in Figure 2.3, at the propellant burning surface there is a noticeable change of slope. The burning surface is shown in the plot as a vertical dashed line passing through the slope-change point. The surface is considered to be at x = 0 position. The region to the left of the dashed line corresponds to the subsurface region of the solid propellant, while the region to the right of the dashed line corresponds to the burnt gas region. The sudden change in the slope is most probably due to the fact that the thermocouple comes in direct contact with gaseous products, which have relatively low thermal conductivity, after crossing the surface of the solid propellant. From the exponential decay of the temperature trace in the sub-surface region, the heat generation in the sub-surface layer can be considered negligible for JA2 propellant.

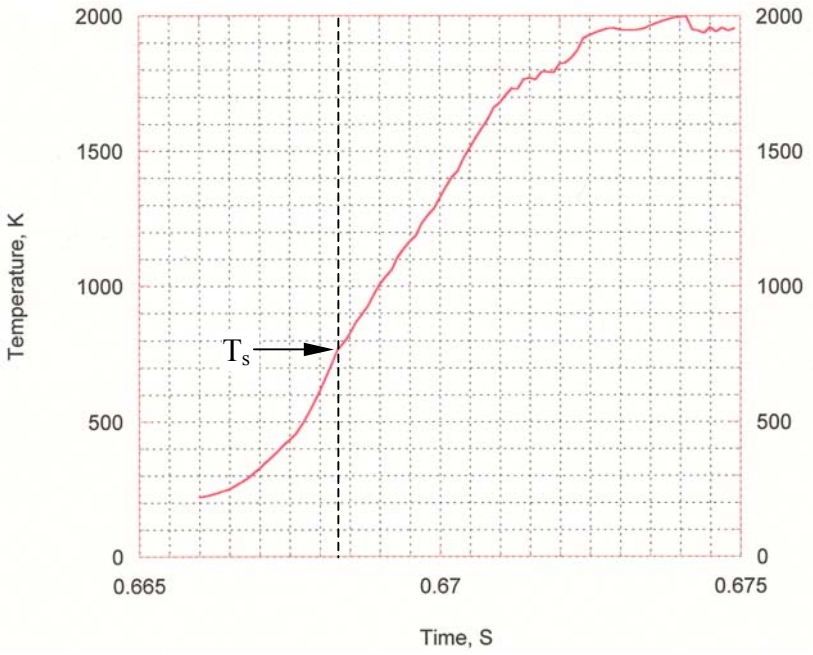

Figure 2.3 A micro-thermocouple trace for JA2 propellant burning at 34.6 MPa (5,000 psig) with initial temperature of 221 K.

Figure 2.4 shows a 3D plot of surface temperature of JA2 as a function of initial temperature (T_i) and pressure (P). For the range of pressure for which surface temperatures were available from experiments, a pressure and initial temperature dependent relationship shown by Eq. (2-9) was chosen for the curve fitting procedure. It should be noted that a linear fit may not be valid for higher pressure data. It is very probable that the surface temperature values start saturating in the high-pressure range. The trend of the surface temperature has been predicted by a relation for double-base propellant by Zenin.[11] The relation used for the curve fitting procedure of the experimental data is given by:

$$T_s = (a_0 + a_1 T_i) + (b_0 + b_1 T_i) P \qquad (2\text{-}9)$$

which, is the equation of a plane. The parameters obtained for Eq. (2-9) are:

$a_0 = 181.0359$ K, $a_1 = 0.7319$, $b_0 = 47.8217$ K MPa^{-1}, $b_1 = -0.0611$ MPa^{-1}

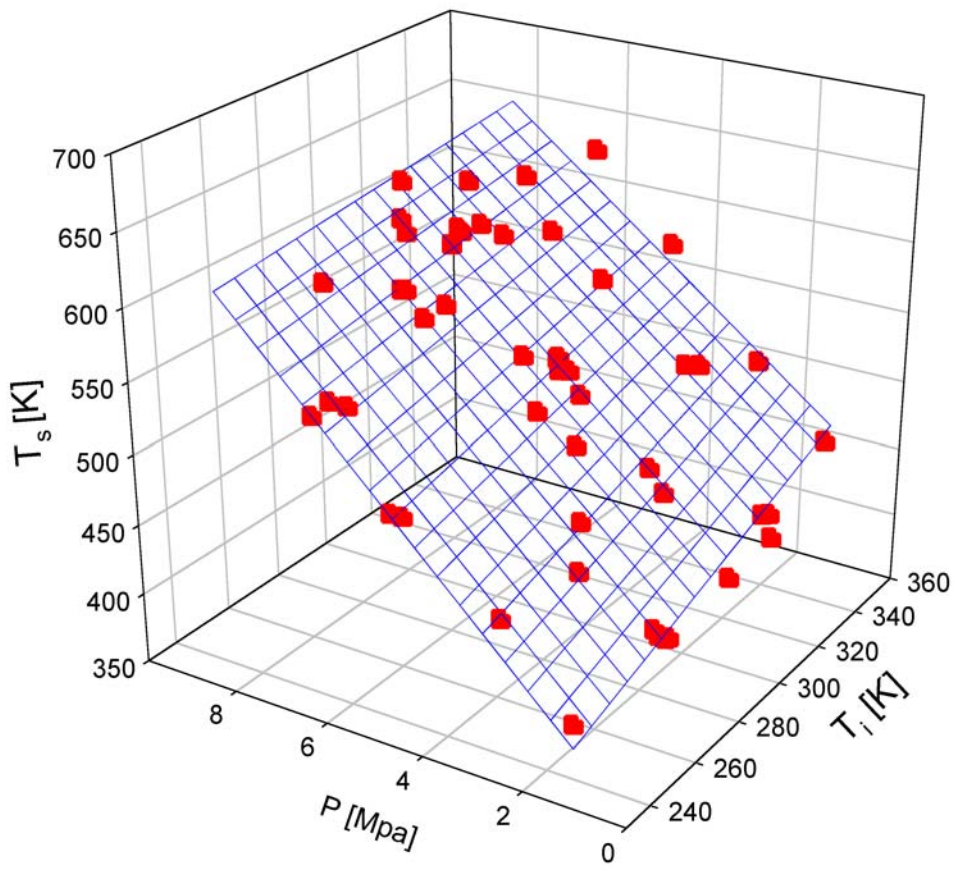

Figure 2.4 Correlation of JA2 propellant burning surface temperature versus initial temperature and pressure.

The activation energy of the JA2 propellant was derived using the experimentally obtained regression rate and the surface temperature. The log of burning rate was plotted against $1/R_u T_s$. The plot is a straight line. The activation energy E_a is obtained from the slope of the line. The plot is shown in Figure 2.5. The experimental data points are scattered around the straight line. The parameters obtained using Eq. (2-10)

$$r_b = A \exp\left[\frac{-E_a}{R_u T_s}\right] \tag{2-10}$$

relating regression rate given in [cm/s] and surface temperature in [K] are:

A = 15.73 cm/s , E_a = 13.4 kJ/mol (this relatively low value corresponds to the r_b at low pressure regime), but at high pressures the activation energy of JA2 is around 47 kJ/mol, based upon Eq. (2-10).

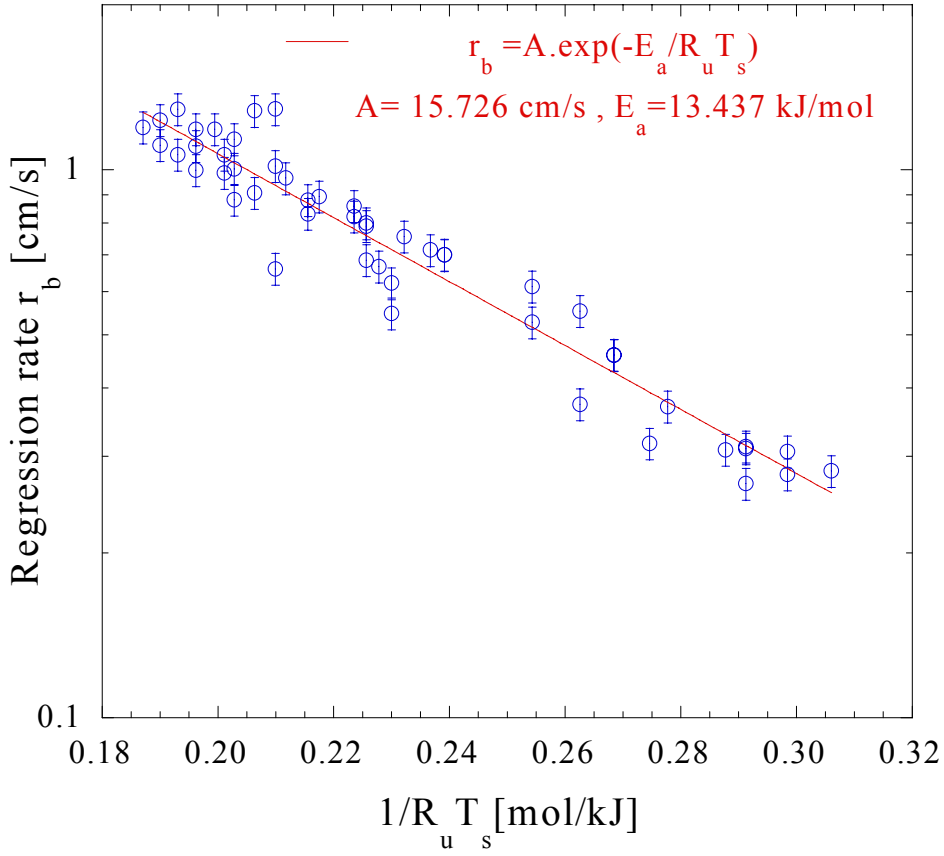

Figure 2.5 Burning rate versus $1/R_uT_s$ for obtaining the Activation Energy of JA2.

2.2.3 Novozhilov Stability Parameters

Novozhilov Stability parameters were determined from the experimental data. The two parameters κ and γ are defined by Eqs. (2-11) and (2-12).

$$\kappa \equiv \left(T_s - T_i\right)\sigma_p \tag{2-11}$$

$$\gamma \equiv \frac{T_s}{T_i} \tag{2-12}$$

Using the correlated results of T_s with P and T_i given in Eq. (2-9), γ is deduced as

$$\gamma = a_1 + a_2 P \tag{2-13}$$

According to Novozhilov Stability criteria [2], a propellant is stable

1. if either $\kappa < 1$ or
2. if $\kappa > 1$, then $\gamma > \gamma^*$, where $\gamma^* \equiv \frac{(\kappa - 1)^2}{(\kappa + 1)}$

From the plot of κ versus T_i and P (Figure 2.6), it is observed that $\kappa < 1$ for some region of the two operating variables [P, T_i], while $\kappa > 1$ for the rest of the region. Therefore, one has to compare γ surface with γ^* surface as well. From the plot of γ and γ^* surfaces versus T_i and P shown in Figure 2.7, it is found that the γ surface is always above the γ^* surface for the ranges of pressure and initial temperature shown on the graph. The γ surface is a plane because of the linear correlation of T_s. If a different function were selected the surface could have been a little different. Thus, it can be concluded that JA2 propellant can burn in a stable manner for the operating range indicated.

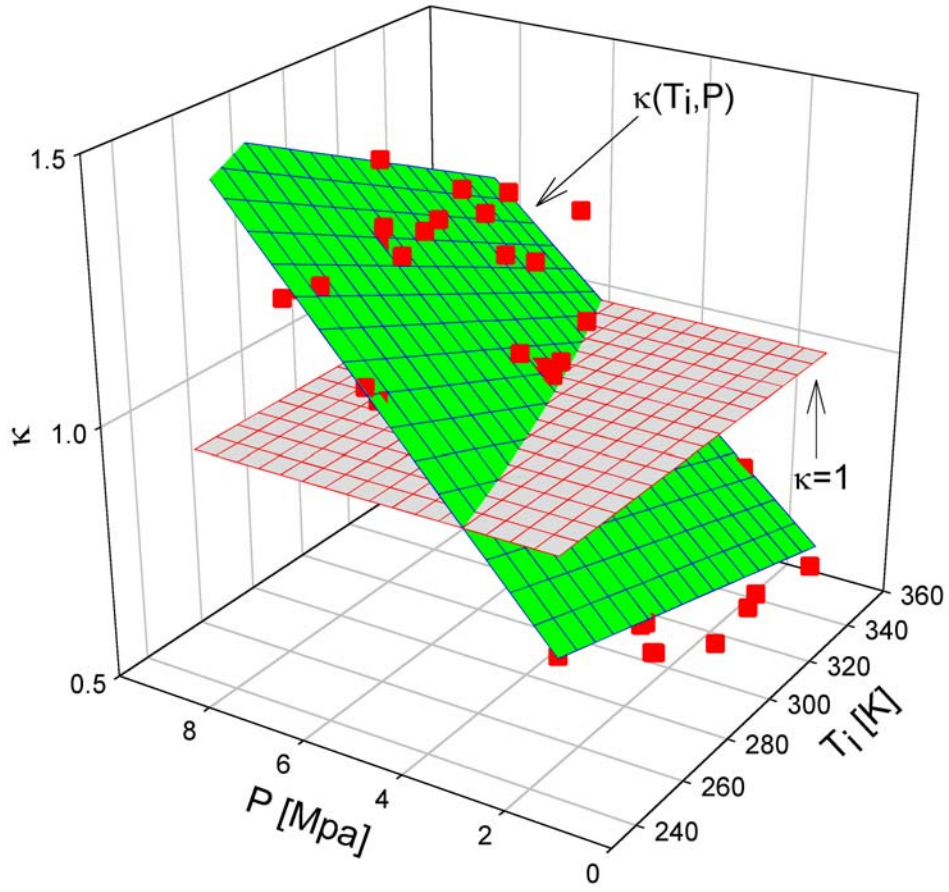

Figure 2.6 Plot of JA2 stability parameter κ versus initial temperature and pressure.

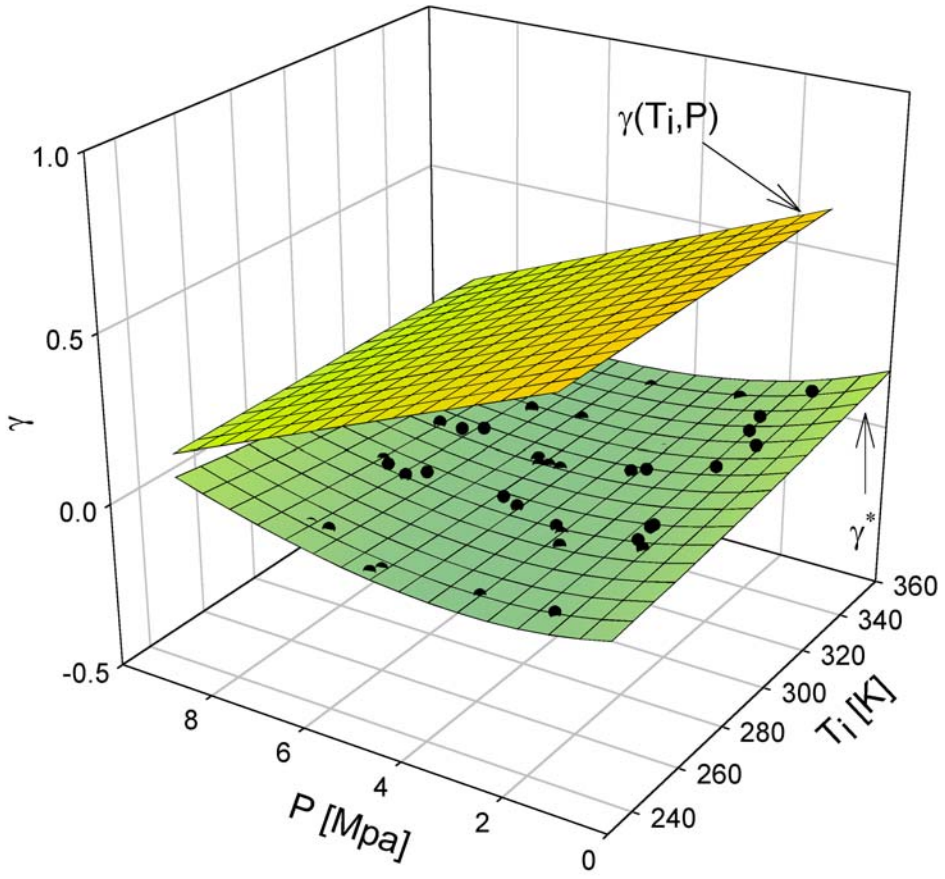

Figure 2.7 Comparison of JA2 stability parameter γ with the γ* surface.

2.2.4 Zel′ dovich Map Construction

The Zel′dovich map of JA2 was constructed using the experimentally obtained parameters and relations. Figure 2.8 shows the Zel′dovich map of JA2 propellant, which essentially shows the temperature gradient immediately beneath the burning surface as a function of regression rate for different P and T_i. The procedure of construction of the Zel'dovich map has been described by Kuo et al.[3] It is worthwhile to note that under very rare situation, the Zel'dovich map is available for a given solid propellant, due largely to the extensive data requirement for broad ranges of test conditions.

2.2.5 Dynamic Burning Simulation Results and Discussion

A dynamic burning simulation was performed using the Zel′dovich approach. Essentially, the Zel′dovich map is used as one of the boundary conditions for the transient energy equation Eq. (2-1). It was assumed that there is no subsurface heat release in JA2, as has been supported by the temperature profiles recorded.

Invariant Imbedding scheme was used in the solution of the non-linear equation with rapidly rising external pressure imposed on the burning environment, to find out various quantities of interest. It has been shown by Kooker and Nelson[12] that this scheme works best for the type of equation in consideration. They have described the invariant imbedding scheme in detail. Theoretical treatment of this method was presented by Meyer.[13] This numerical scheme is unconditionally stable.[12] It is first-order accurate in time and second-order accurate in space i.e., $O\left(\Delta\tau, \Delta\eta_{max}^2\right)$.

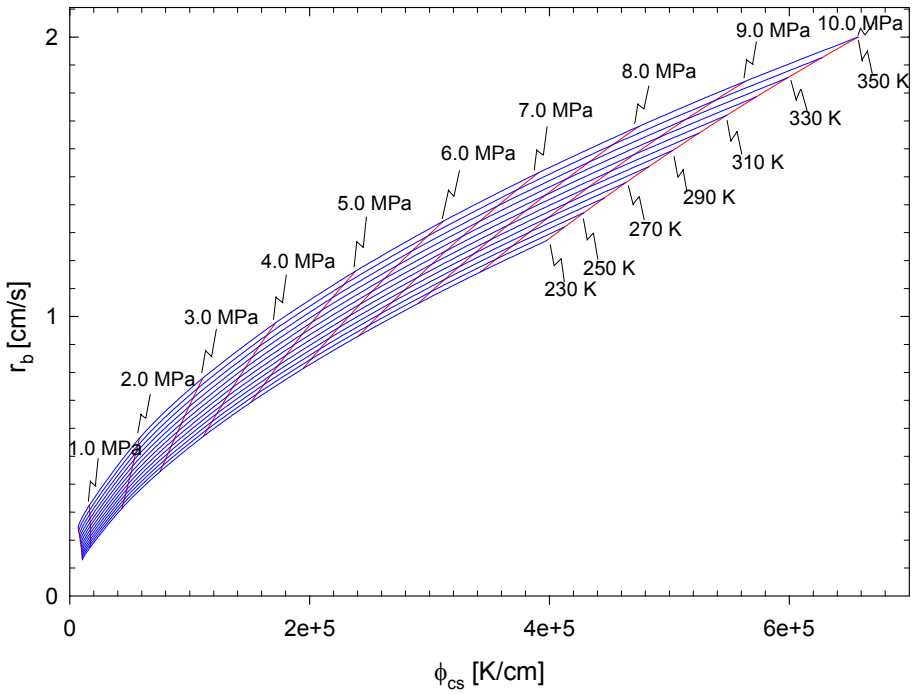

Figure 2.8 Zel'dovich Map of JA2 propellant.

The time and distance variables (t and x) were made dimensionless and the calculations were performed in non-dimensional form. Later on the quantities were reverted to dimensional form. Since the problem involves a thermal profile, which may have very steep gradients near the burning surface, the spatial mesh was closely spaced in this region (i.e., $\Delta\eta << 1$). A 231-grid point system [21 points in the region $-0.01 \le \eta \le 0$; 30 points in the region $-0.10 \le \eta \le -0.01$; 50 points in the region $-2.00 \le \eta \le -0.10$; 130 points in the region $-15.00 \le \eta \le -2.00$] was selected for the calculation. The different quantities used in the calculations are described below.

$r_o = 0.2476$ cm/s, $T_{s,o} = 389.3$ K, $T_i = 298.0$ K,

$t_c = 21.53$ ms, $\tau \equiv \frac{t}{t_c} = t\left(\frac{r_o^2}{\alpha_c}\right)$, $\tau_i = 0.0$, $\tau_f = 3.0$, $\Delta\tau = 0.01$

$x_c = 53.31$ μm, $\eta \equiv \frac{x}{x_c} = x\left(\frac{r_o}{\alpha_c}\right)$, $\eta_o = -15.00$,

$\alpha_c = 1.32 \times 10^{-7}$ m^2/s,

$P_o = 1.00$ MPa, $\Delta p_{ndm} = 2.5$ (non-dimensional)

In the following sections, the results of the simulation are presented. The purpose of the study was to compute the burning rate response to a rapidly increasing pressure excursion. For that, ramp type profiles as described by the equation below were selected with different initial pressurization rates. The maximum pressure is same for all the cases. The τ_{Ramp} is different for the different cases.

The pressure profile is a ramp starting at P_o and rising at a certain pressurization rate dP/dt and then remaining at constant pressure of $P_o[1.0 + \Delta p_{ndm}]$ after $\tau = \tau_{Ramp}$ defined by

$$\mathbf{P(t)=P_o[1.0+\Delta p_{ndm}\,(\tau/\tau_{Ramp})]} \qquad \textbf{for } 0 \le \tau \le \tau_{Ramp} \tag{2-14}$$

$$P(t)=P_o[1.0+\Delta p_{ndm}] \qquad \text{for } \tau > \tau_{Ramp}$$

Six different pressure profiles were chosen with initial pressurization rates of 0.1, 0.5, 1.0, 5.0, 10.0 and 20.0 GPa/s.

Figure 2.9 shows R, the ratio of dynamic burning rate to burning rate calculated, using the pressure profile and steady-state burning rate expression given by Eq. (2-1). It can be noted that at first, the ratio R falls below one, indicating that the thermal wave, which controls the burning rate does not respond instantaneously to the increasing pressure. One can observe a slight increase in the burning rate near the initial part of the profile. The maximum overshoot value of R is around 1.1, signifying a weak dynamic burning effect of JA2 propellant. After sometime R reaches the steady-state value of unity for all cases studied.

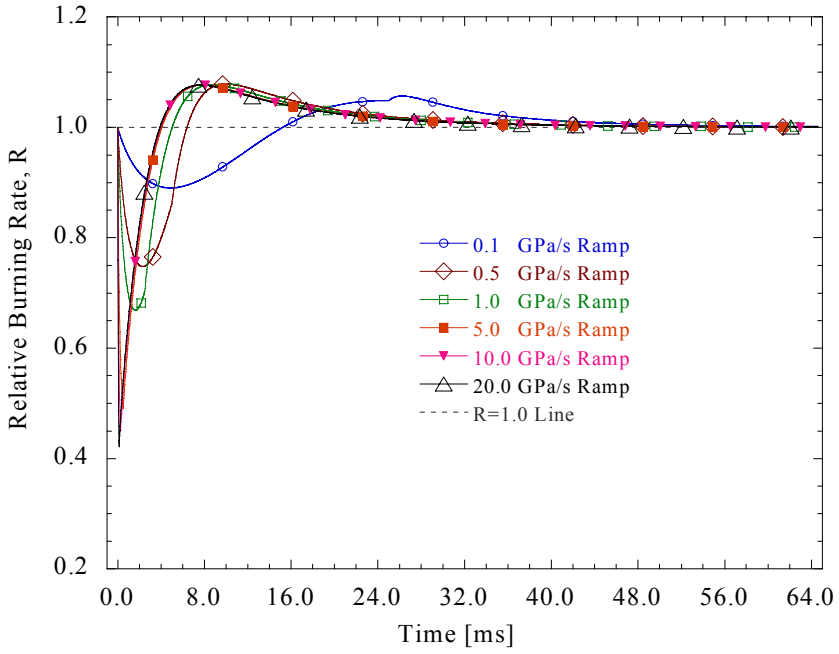

Figure 2.9 Calculated time variation of the ratio of dynamic burning rate to steady-state burning rate based upon the instantaneous pressure.

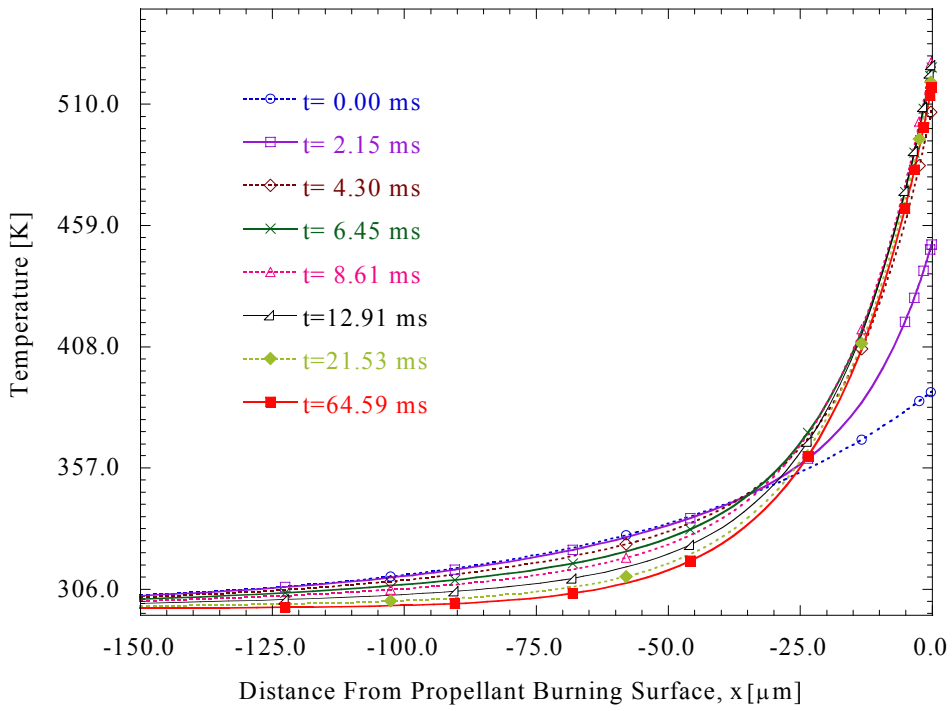

Figure 2.10 A set of calculated temperature profiles in the condensed phase of JA2 propellant as a function of time and distance.

Figure 2.10 shows the development of the sub-surface temperature profile in JA2 for different times in the dynamic burning event under the pressure profile with initial pressurization rate of 1.0 GPa/s. It can be observed that the temperature profiles crossover during the development process in the low-temperature region. The gradients are higher during the times when the burning rate is higher than the steady-state burning rate. This observation matches with the work of Watson, et al.[10] on interrupted burning of JA2 propellants.

CHAPTER 3 Combustion Behavior of Two Opposing JA2 Propellant Strands

To simulate high loading density conditions two JA2 propellant strands are burned in close proximity. Figure 3.1 shows the configuration of the two opposing burning strands with their flames confined between the propellant surfaces.

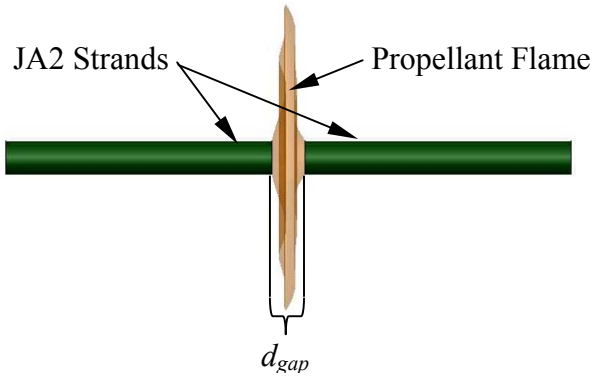

Figure 3.1 Sketch of opposing strands of JA2 solid propellant burning with a flame inbetween.

3.1 Theoretical Considerations

The burn rate of a solid propellant is sensitive to many factors and conditions. Of these conditions the heat transferred to and from the propellant surface is of most importance. The energy flux balance at the burning surface of a solid propellant is represented in Figure 3.2 and given by:

$$\lambda_p \left.\frac{dT}{dx}\right|_- = \lambda_g \left.\frac{dT}{dx}\right|_+ + \rho_p r_b Q_s + I_f \qquad (3\text{-}1)$$

where λ_p is the solid-phase thermal conductivity, λ_g is the gas-phase thermal conductivity, r_b is the burning rate, Q_s is the heat release at the surface, ρ_p is the density of the propellant, $(dT/dx)|_-$ is the sub-surface temperature gradient, $(dT/dx)|_+$ is the gas-phase temperature gradient, and I_f is the heat feedback due to flame radiation.

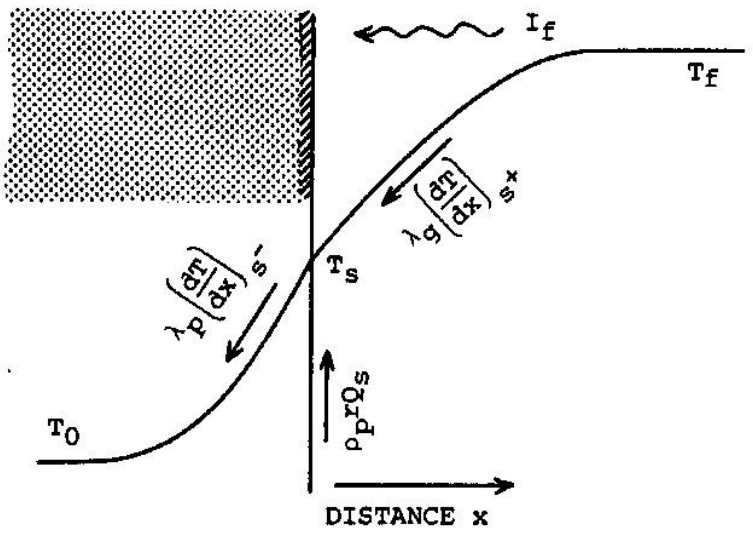

Figure 3.2 Schematic of the heat balance at a steadily burning surface.[14]

Eisenreich, et al.[15] used a simplified approach to study the burning of solid propellants that also takes into account the radiation and heat release. Equation (3-2) is deduced from their simplified heat transfer balance:

$$r_b = \frac{Q_s + I_f}{\rho_p \left(c_p \left(T_s - T_\infty \right) + L - \sum_i q_i \right)} \tag{3-2}$$

where Q_o is the heat feedback from the flame zone to the burning surface due to conduction, T_∞ is the initial temperature, T_s is the surface temperature, L is the heat of phase transition, Σq_i is the heat of chemical reactions in the solid, c_P is the specific heat, and ρ_p is the propellant density.[14] When combining the phase transition energies and the chemical reactions, Eq. (3.2) reduces to

$$r_b = \frac{Q_o \left(P, d_{gap} \right) + I_f}{\rho_p \left(c_p \left(T_s - T_\infty \right) - Q_s \right)} \tag{3-3}$$

This equation can also be derived directly from Eq. (3.1) with the subsurface energy flux replaced by the internal energy increase across the thermal wave inside the solid propellant. Upon further investigation, Eisenreich et al.[15] discovered Q_o corresponds to the pressure raised to

the power n, which is the pressure exponent of the burn rate. Q_o is also a function of the gap width for the double strand configuration in this study. As the gap width (d_{gap}) is reduced the temperature gradient at the burning surface becomes steeper when the flames of the two burning propellant strands are still confined in the gap space. Radiation energy flux can also be affected by gap spacing since the shape factor is a function of the geometry. When two strands of solid propellant are in close proximity there is limited space for the propellant flame to extend from the propellant surface. In addition the burning surface can radiate energy to the opposite propellant surface. Therefore, gap spacing can affect the radiation flux level. In general, the low-pressure data are of particular interest since high loading density conditions correspond to the initial packing of the propellant grains in the cartridges of any artillery systems.

3.2 Experimental Approach

To study the steady-state combustion behavior of JA2 under high loading density conditions, parameters of the experiment have to remain constant. Therefore, a steady-state experiment holding pressure and gap width constant was developed. Holding these two parameters constant made the measurement of the burn rate easier and more reliable than a transient experiment. To hold the pressure constant a surge tank coupled with a pressure transducer and a computer controlled solenoid valve were used with a purge flow. To hold the gap width constant a specially deigned test rig along with a control feedback loop and control optics were used. The combination of these components provided a steady-state experimental apparatus shown in Figure 3.3.

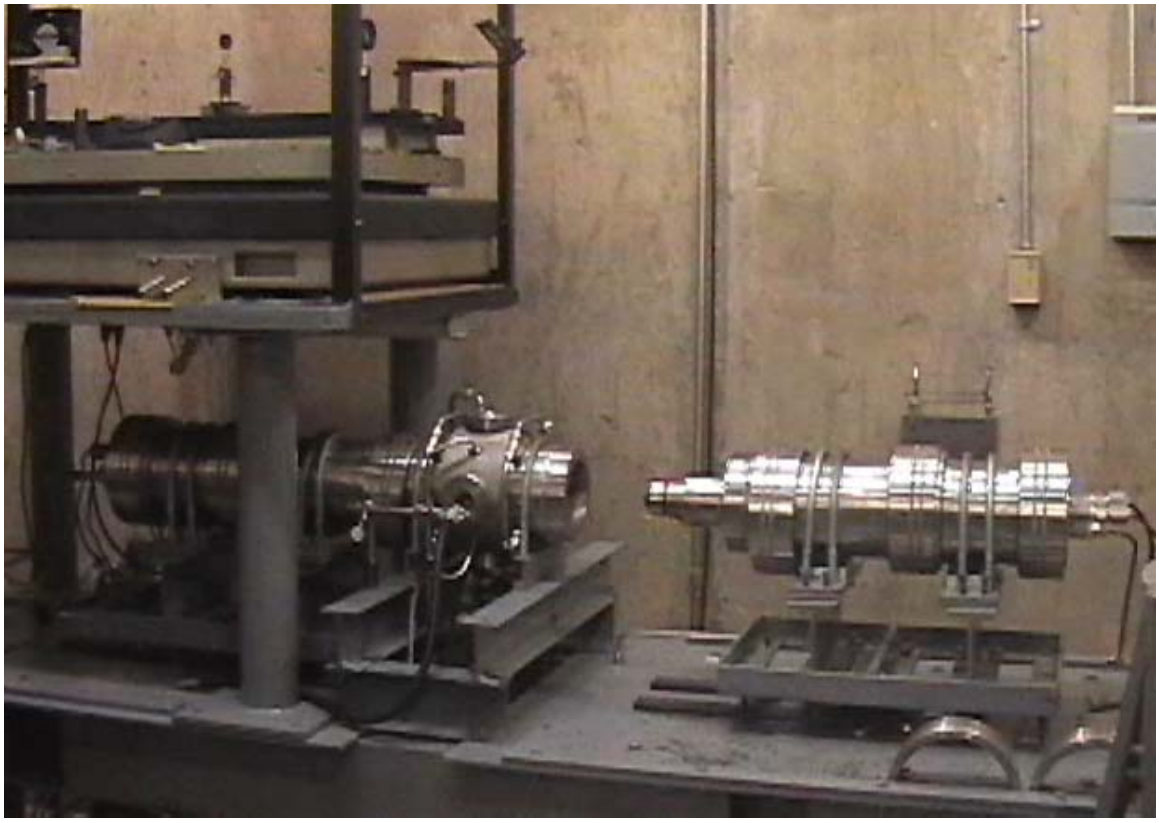

Figure 3.3 Constant gap width strand burner experimental setup.

3.2.1 Double-Ended Windowed Strand Burner

To partially simulate close gap burning conditions experienced in the ballistics of gun systems, a double-ended windowed strand burner (DEWSB) was utilized. The DEWSB allows the propellants to be fed toward each other to keep a constant gap as they burn. This device was designed to operate under a controlled manner so that data can be collected for a constant specified gap width for a period of time (on the order of 10 seconds). The DEWSB consists of a high-pressure vessel for housing two identical drive systems adjoined to a center windowed combustion chamber, a purge feed system, a surge tank to keep the chamber pressure at a constant level, and an exhaust system for the burned products and purge gas. A photograph of the DEWSB is shown in Figure 3.4.

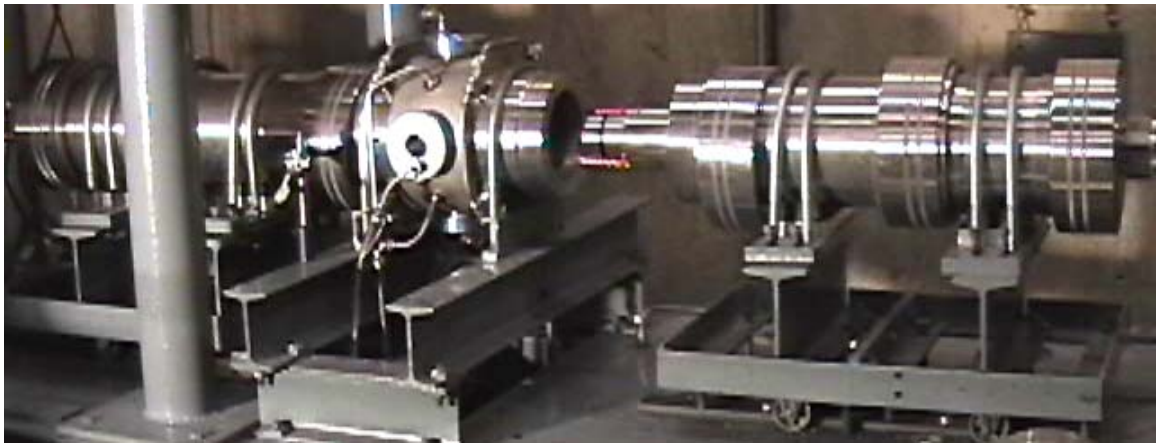

Figure 3.4 Double-ended windowed strand burner.

3.2.1.1 High-Pressure Vessel

The high-pressure vessel contains each of the drive systems and the center combustion chamber. It is made up of five stainless steel cylinders and two endplates, held together by flangeless couplings with o-ring seals between each. The stainless steel cylinders containing the drive systems are mounted to heavy duty rolling carts with height adjustments, while the center combustion chamber remains stationary. The reason for mounting the linear drive systems to rolling carts is so the propellant strands can be loaded easily for each test. The flangeless couplers were chosen for ease of operation in the horizontal configuration.

3.2.1.2 Linear Drive Mechanism

The drive system for each propellant strand is composed of a stepper motor, a linear ball screw, a linear potentiometer, a nozzle, and a propellant strand holder (see Figure 3.5).

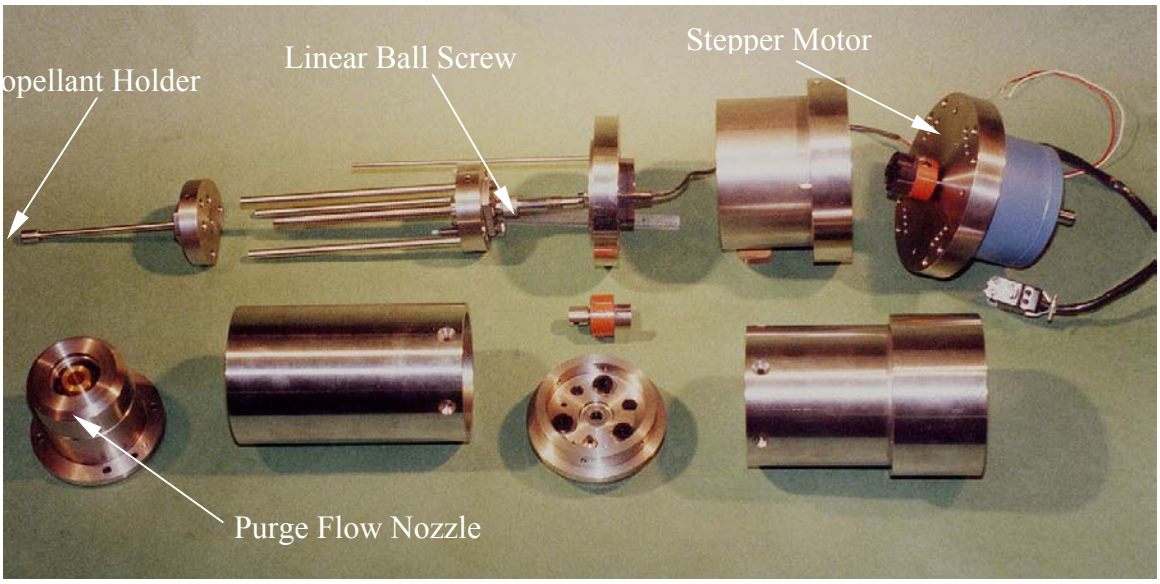

Figure 3.5 Linear drive internal parts.

The stepper motors are operated with micro stepping capability at 2,000 – 3,200 steps per revolution at 20 revolutions per second. The linear ball screw is used to convert the rotational motion of the motor a to linear motion. The ball screw has a pitch of 2 mm. The combination of the stepper motor capability and the pitch of the linear ball screw allows the propellants linear displacement to be on the order of 0.625 – 1.0 μm per step, which is very small compared to the burning surface roughness. A linear potentiometer is used in the system to measure the displacement distance of the propellant sample showing the instantaneous length of the propellant, which has been fed into the flame zone. The output of the linear potentiometer is given as a voltage signal in the range of 0 to 5 volts. The output voltage corresponds to a distance, based upon the in situ calibration data. The nozzle is used for purge flow. The nozzle has a center port to allow the propellant holder and sample to travel through, and smaller holes on the annular region for purge gas to pass through. On the end of this nozzle there is a graphite element to straighten the flow around the propellant strand and to serve as a high-temperature material for protecting the stainless steel nozzle. Finally, the propellant is held in place with a

thin needle stuck into its base and an annular graphite guide component to keep the propellant strands in line with each other.

3.2.1.3 Purge Gas Control System

Nitrogen purge flow is used in the DEWSB for three main purposes. First, the purge gas is used to pressurize the combustion chamber to the desirable operating pressure. This is accomplished by remotely controlling the inlet and outlet flows. Second, the purge gas flow lines enter the combustion chamber through the rear end of each linear propellant drive. This arrangement prevents the combustion product gases from flowing into the compartment containing the linear drive system and causing possible damage to any electronic components. Most importantly, the purge gas flow prevents the flame from spreading down the lateral side surface of the propellant sample. Furthermore, the purge gas is used to keep the observation windows clear of exhaust and combustion products during each test. An overall flow diagram is shown in Figure 3.6.

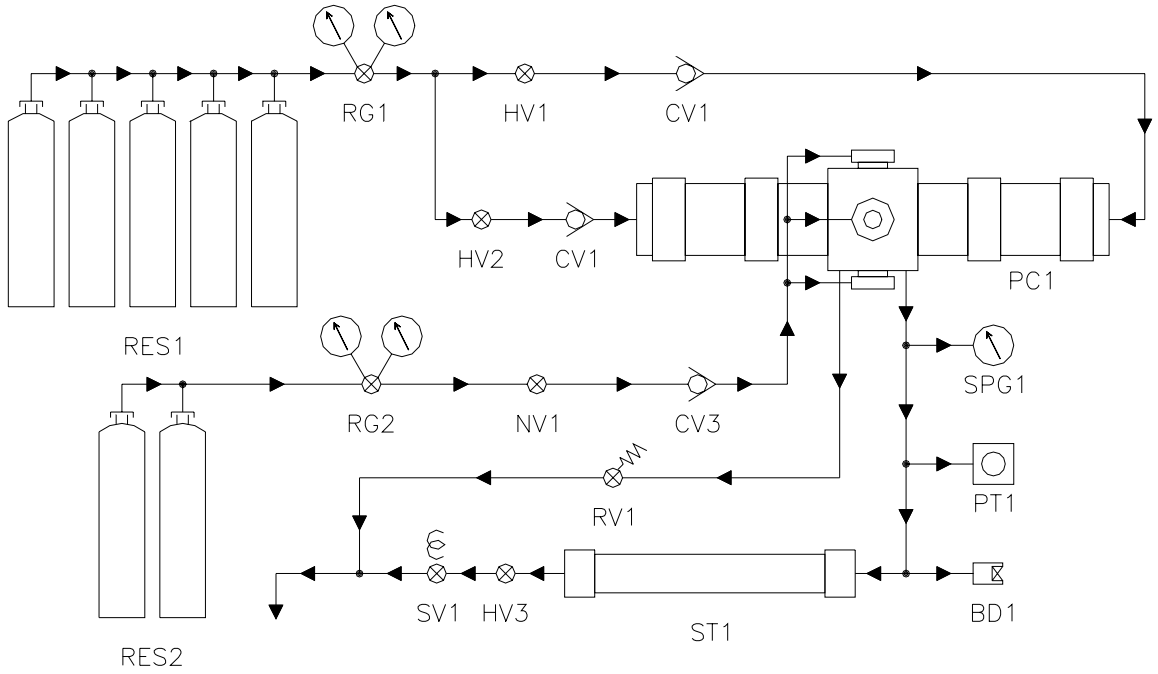

Figure 3.6 Purge system flow diagram.

Table 3.1 shows the symbol meanings and total number of each part used in the purge flow system.

Table 3.1 Flow diagram symbols.

Symbol	Meaning	Total Used
RES	Reservoir	2
RG	Regulator	2
HV	Hand Valve	3
CV	Check Valve	3
PC	Pressure Chamber	1
NV	Needle Valve	1
SPG	Static Pressure Gauge	1
PT	Pressure Transducer	1
BD	Burst Disc	1
ST	Surge Tank	1
RV	Remote Valve	1
SV	Solenoid Valve	1

The existing exhaust system was comprised of eight ports leading from the perimeter of the center combustion chamber to a surge tank. Initial testing of JA2 propellant strands showed too much combustion product gas flowing radially outward in the central section of the DEWSB. This prohibited a clear black-and-white contrasting image needed by the computer code for gap width measurement and control. It was determined that a shadowgraph effect on the background image can be influenced by the combustion product gas flow and the temperature gradient in the gas mixture. To rectify this problem, an assortment of solutions was tried. It was decided that discharge of more exhaust product from the center combustion chamber could help to obtain an acceptable background image around the propellant sample. Four new exhaust ports were drilled around the center of the combustion chamber to allow greater discharge rate of the combustion products. These modifications were effective in obtaining suitable propellant sample image for control application and can be seen in Figure 3.7.

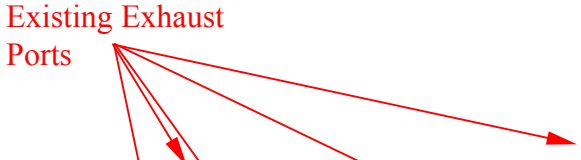

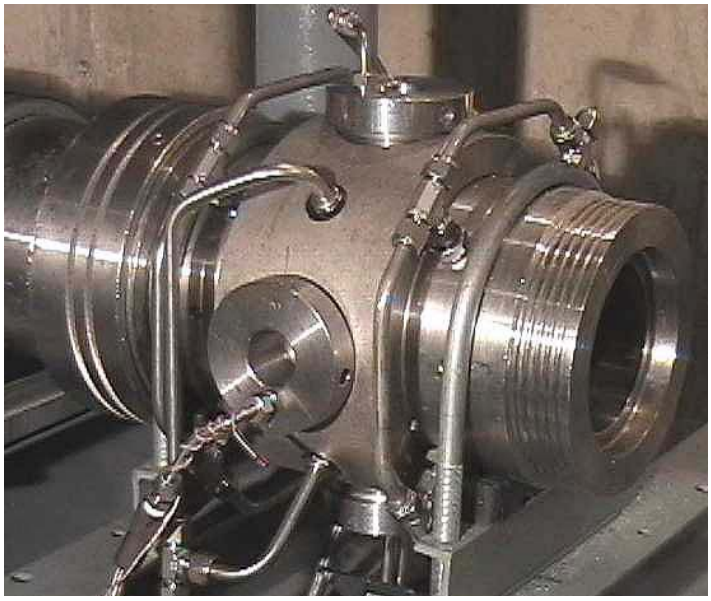

Figure 3.7 Center combustion chamber with exhaust ports.

Low pressure testing was conducted using a large volume surge tank rated up to 3.45 MPa. With a larger volume surge tank the ability to keep the operating pressure constant was easier. However, this surge tank is only rated for 3.45 MPa and desired testing pressures are up to 10.34 MPa. A smaller volume high-pressure surge tank rated up to 31.03 MPa was installed on the base of the test frame seen in Figure 3.8. Since the volume of the new surge tank is relatively small compared to the initial surge tank, it will be more difficult to control the operating pressure. It was decided to use a pressure transducer signal and a data acquisition card to control the closing and opening conditions of the existing solenoid valve.

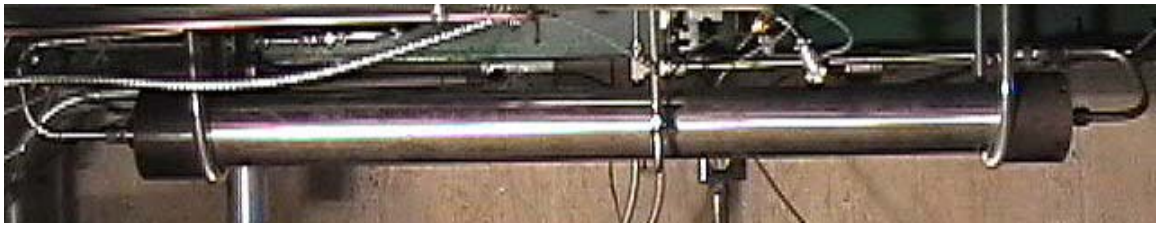

Figure 3.8 High-pressure surge tank.

3.2.2 Optical Measurement and Gap Width Control System

Due to the complexity of the burning surface geometry and rapid propellant regression rate, the feeding system needs to be computer controlled to keep a constant average gap width throughout the duration of the test run. This is performed using live video images captured through one of the four port windows, and processed nearly real-time by imaging software to determine the instantaneous space-averaged gap width. Once the gap width is known, it is compared to the desired gap width and an appropriate signal is sent to the linear feed control system to control the motor feeding rate.

A contrasting image between the propellant strands and the background is desired to automate the measurement of the gap width between the two opposing propellant strands. In order to accomplish this goal, an optical laser system was chosen. The system consists of four main components, a laser, optical lenses, a CCD camera and a video capture card. The laser provides a high intensity monochromatic light source for contrasting the propellant image with the burned gas background. This image is recorded by a camera, which sends the image to a frame grabber installed in a personal computer. The overall online optical gap width control system is shown in Figure 3.9.

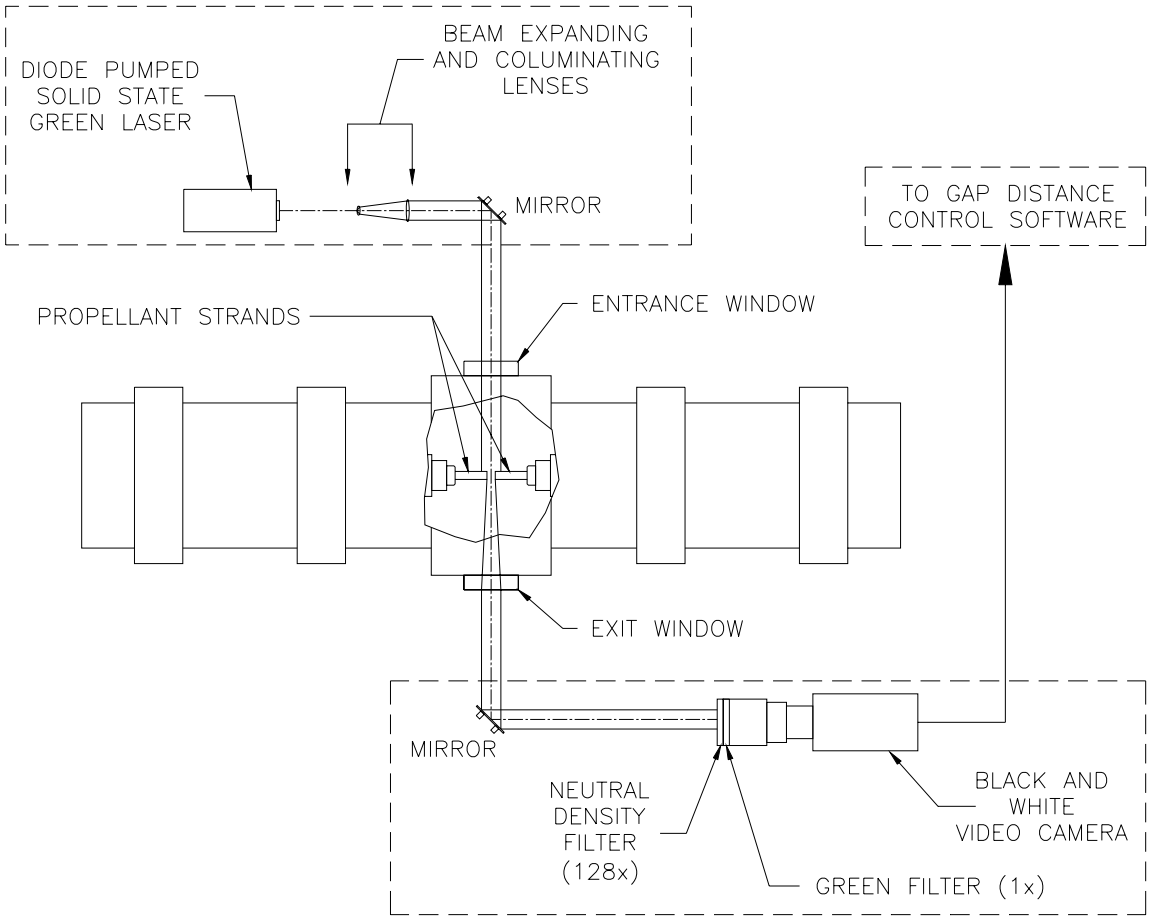

Figure 3.9 Schematic diagram of the online optical gap width control system.

3.2.2.1 Solid-State Laser

The laser chosen is a 20-mW diode-pumped solid-state laser from Lasermate Group, Inc. The wavelength of the laser is 532 nm (green). This laser wavelength and power were chosen to offset the wavelength (~700 nm) and intensity of the propellant flame. It is a low-cost high-performance laser module system. It comes complete with a key lock and toggle switch for safety. The beam divergence is only 1.4 mrad and the beam diameter is 1 mm. Since the beam diameter is small, optical lenses are required to expand and collimate the laser beam before passing it through the combustion chamber.

3.2.2.2 Optic Lenses

The center combustion chamber window has a diameter of 25.4 mm. However, since the laser beam diameter is only 1 mm it needs to be expanded and then collimated. A Galilean style beam expander was selected for this purpose. This configuration is a much shorter distance than a Keplerian beam expander.[16] Two lenses are required to accomplish this. The first lens has a negative focal length, $-f_1$. The second lens has a positive focal length, f_2. Spacing these lenses apart at a distance equal to the sum of the two focal lengths gives an expanded and collimated laser beam. From Figure 3.10, y_1 is the laser beam radius, 0.5 mm, and θ_1 is the laser beam divergence angle, 0.7 mrad. f_1 is the focal length of the plano-concave expanding lens, and f_2 is the focal length of the plano-convex lens.

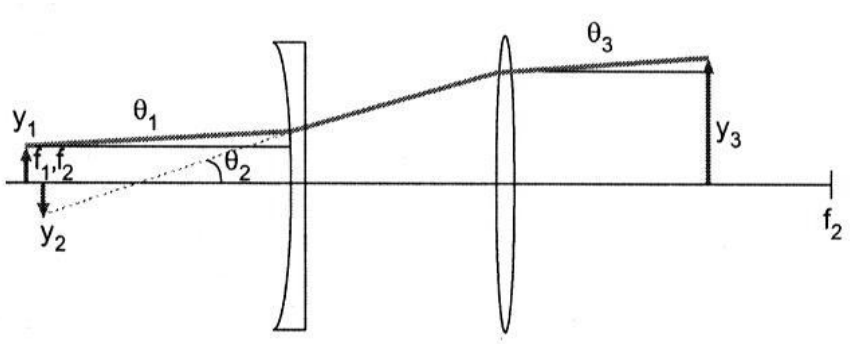

Figure 3.10 Galilean expanding and collimating diagram.[16]

The focal length of the two lenses is chosen through standard lens calculations based upon the following equation:

$$\frac{y_3}{y_1} = \frac{f_2}{|-f_1|} \qquad \textbf{(3-4)}$$

The final beam radius, y_3, must be 12.25 mm so the expansion ratio found was 24.5. For this expansion ratio the focal length of the two lenses must be different by at least a factor of 24.5. A –9 mm focal length plano-concave expanding lens, and a 300 mm focal length plano-convex collimating lens were chosen shown in Figure 3.11.

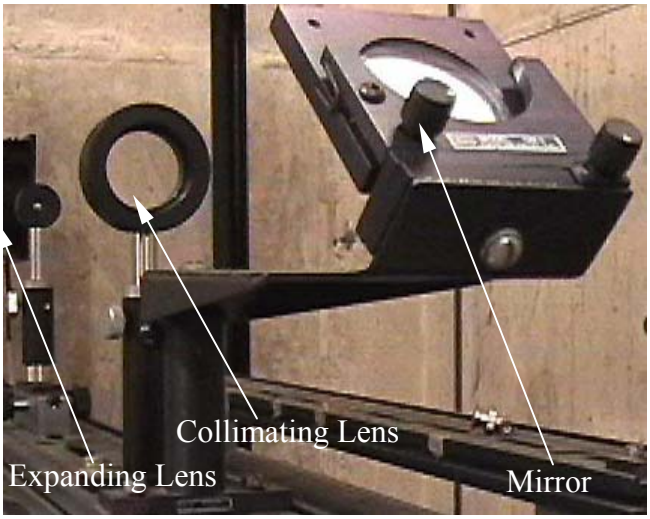

Figure 3.11 Optical lens setup.

This combination gave an expansion ratio of about 33, so the final beam radius was 16.5 mm. Since the laser has a Gaussian distribution from the center, this over-sizing design allows the most intense part of the laser beam through the window.

To conserve space an optics table was assembled above the left side of the DEWSB. Therefore, the laser beam needed to be reflected down to the top center combustion chamber window. A first surface mirror was used to do this. After the beam passes through the combustion chamber it gets reflected back towards the wall for safety with another first surface mirror. A CCD camera then records this image.

3.2.2.3 CCD Camera

The camera used is a black-and-white TM-200 Pulnix high resolution CCD camera. This camera was selected because its sensitivity is closest to the wavelength of the laser (see Figure 3.12). This sensitivity can help reduce a portion of the propellant flame image emission, and give a better contrasting image.

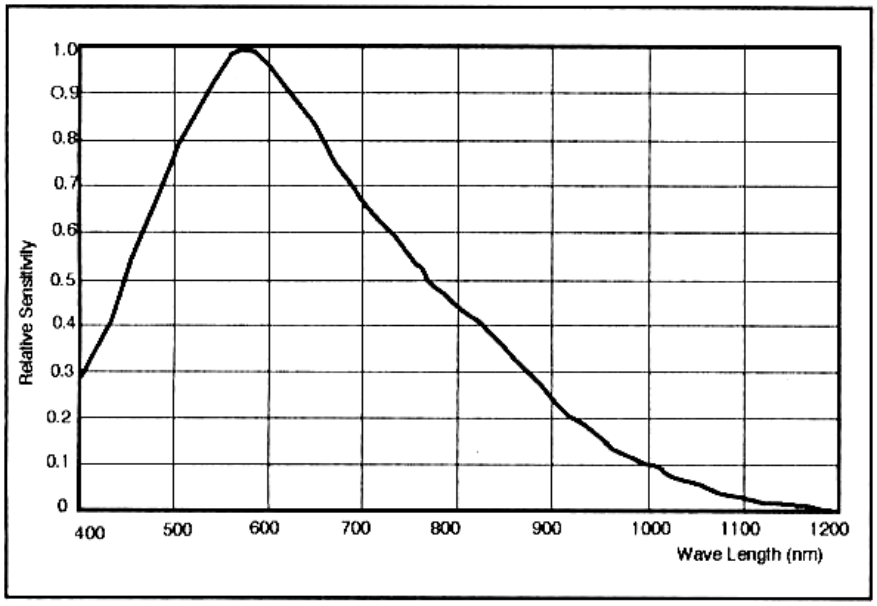

Figure 3.12 Pulnix TM-200 sensitivity to wavelength.

A macro video zoom lens was used together with the CCD camera. It has the focal capability from 18 to 108 mm. High zoom abilities are provided to focus as closely as possible to the burning surface of the propellant. The closer zoomed to the burning surface of the propellant; the more accurately a space-averaged gap width can be obtained. Hoyt neutral density, green, and polarizing filters were also used. A total of three neutral density filters (two 8x and one 2x) was combined in usage, this reduced the intensity of the light coming into the camera by 128x. The green filter eliminated other flame emission colors. Finally, the polarizing lens reduced the glare reflected from the mirror into the camera. The camera is positioned near the back of the experiment for laser safety and damage control purposes.

3.2.2.4 Image Acquisition Card (Frame Grabber)

In order to obtain the instantaneous image from the camera and send it to the image processing software, an image acquisition card is required. Since National Instruments LabVIEW is the software being used for image processing, a National Instruments PCI 1411 single-channel color or monochrome image acquisition card was selected. This card is

compatible with the analog video output from the black-and-white Pulnix camera. It is capable of partial image acquisition with a programmable region of interest. There is a TTL external trigger as well. This feature is used by the image processing software to send a signal from the computer to a relay that switches the high-speed motor control circuit on and off. A computer with an AMD Athlon 1700 processing chip, 256 megabytes of RAM, 40-gigabyte hard drive, and a Windows 2000 operating system, was used to operate the image acquisition card and the image processing software. This was the best choice for a high-speed computing system capable of approximate real-time analysis and control.

3.2.2.5 Image Processing Control Loop

National Instruments LabVIEW software was used to process the black-and-white image and determine whether or not the high-speed control circuit should be switched on or off. More specifically, IMAQ Vision as a subset of LabVIEW was used. Opposed to the grayscale image from the camera, a contrasting black-and-white image was achieved with this software. From this image, the space-averaged gap width was measured and utilized for comparison with a user specified gap width; the results of this comparison determine the switching option for the high-speed motor control. Figure 3.13 shows the overall image processing control loop with three main steps involved.

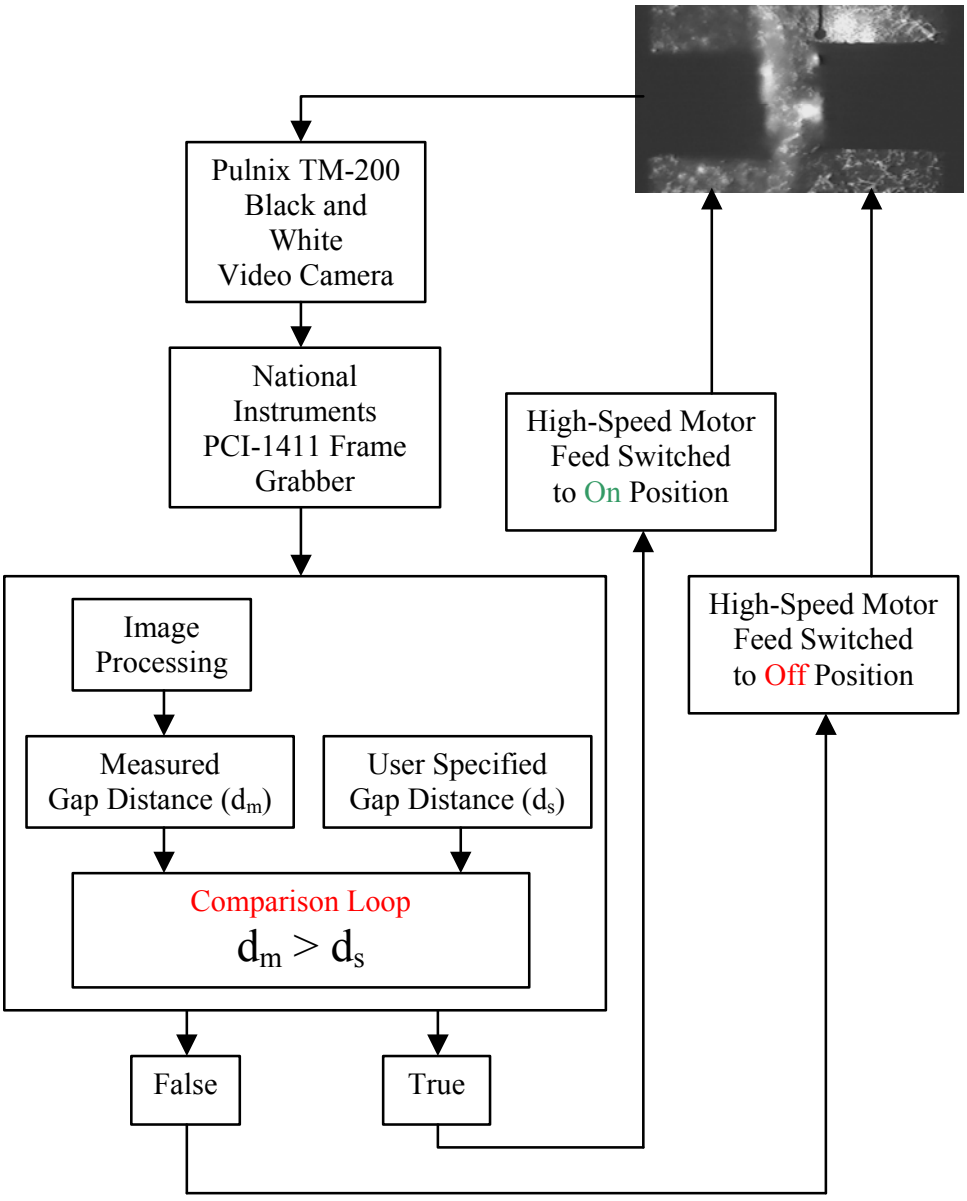

Figure 3.13 LabVIEW Image processing control loop.

3.2.2.5.1 First Step of Image Analysis

A raw image that is recorded by the black-and-white camera is in grayscale. Figure 3.14 is an example of the initial image before processing. The two propellant strands are noticeable, however, there is not a clear contrast between the propellant and the background. This is a result of the temporary accumulation of combustion product gases adjacent to the burning propellant surfaces. A shadowgraph effect of the gas phase mixture in the viewing area is seen (as a

honeycomb structure) due to the high intensity of the laser light. The shadowgraph effect prohibits a good gap width measurement from the raw image.

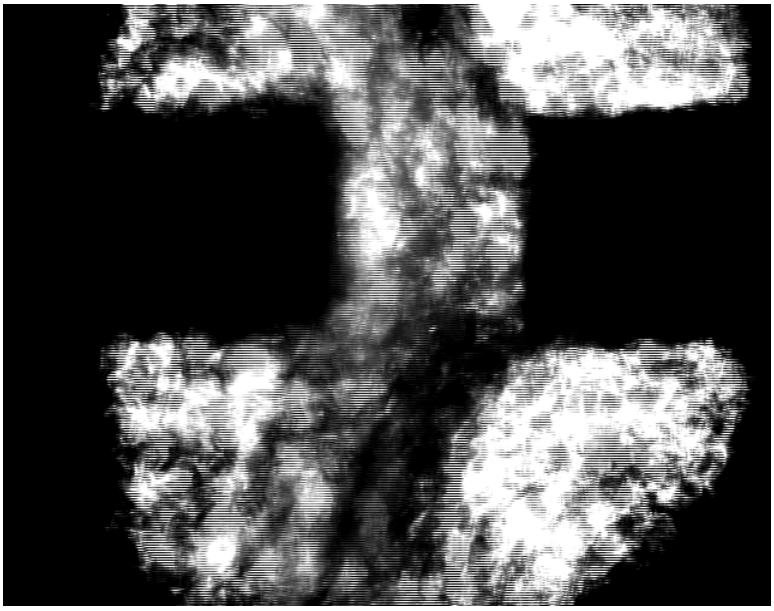

Figure 3.14 A typical instantaneous raw image recorded by the black-and-white camera (6.35-mm diameter strands).

The first action in the image processing is the application of thresholding. The colors of the image are ranged in a scale of grays, from 0 (black), to 255 (white). Here, specifying a threshold level modifies the distribution of the background intensity. For all pixels with gray level below the specified threshold level are set to white. In other words, all the shades of gray between dark gray and white become white. The pixels having gray levels above or equal to the specified threshold level are set to black. The selection of the threshold gray level is based upon the criterion that the end surfaces of the strands are more properly simulated rather than the lateral surfaces of the two opposing strands. Some artificial roughness of the lateral surface could be introduced by the binary treatment; however, the end surfaces are smoother than the lateral surfaces. This provides a more accurate measurement of the average gap width. After

this binary treatment, some other LabVIEW Vision Builder functions were used to improve the contrast, producing a uniform black-and-white image seen in Figure 3.15.

Figure 3.15 LabVIEW processed image.

3.2.2.5.2 Second Step of Image Analysis

After treating the image, the code calculates the space-averaged gap width between the two burning propellant strands. In order to do this, a region of interest is selected by the user, which includes the major portion of the gap space plus the unburned portions of the two propellant strands, as indicated by the green rectangle in Figure 3.16.

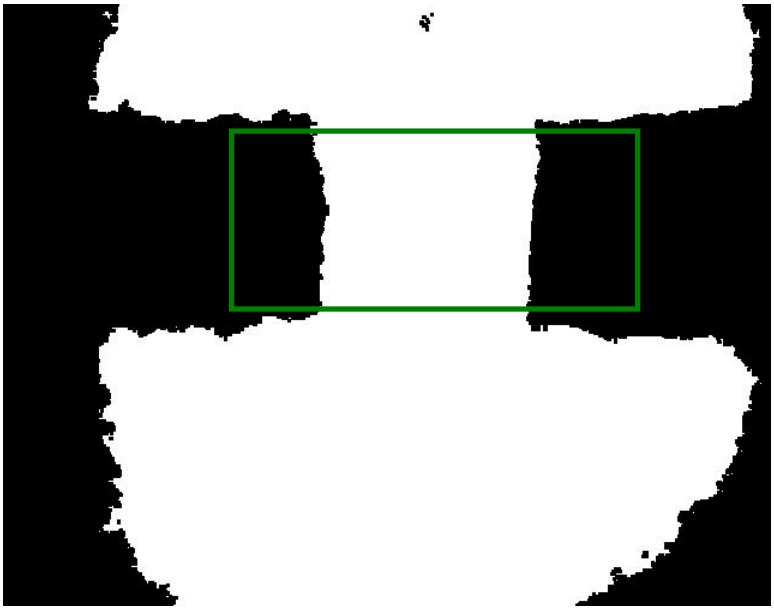

Figure 3.16 Region of interest marked by green rectangle.

Afterwards, a horizontal line is drawn per pixel height in the selected region of interest. The exact number of pixels in the vertical direction depends upon the height of the region of interest. Then, on each horizontal line, the edges (shown as red dots in Figure 3.17) at the solid/gas interfaces are determined. Their location corresponds to the abrupt contrast change from black to white or vice versa.

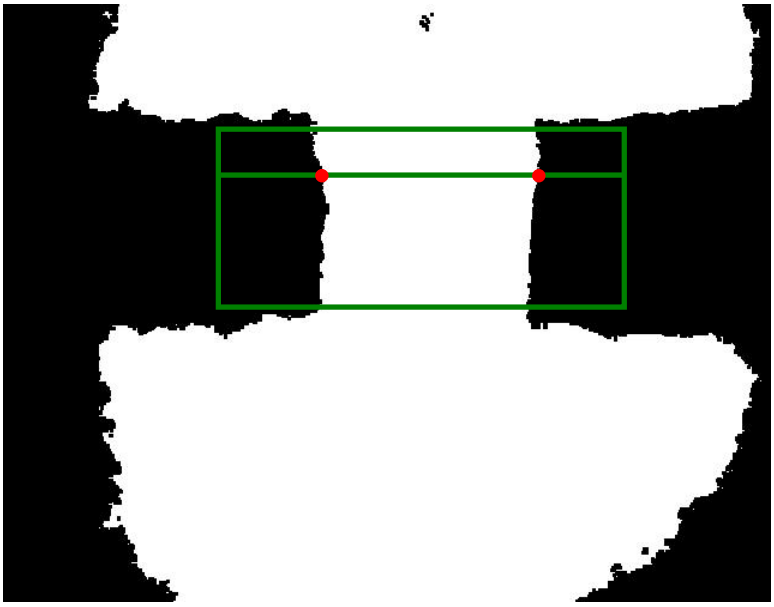

Figure 3.17 Contrasting solid/gas interfacial location determination.

After this operation, two distances d_1 and d_2 are determined (see Figure 3.18). By subtracting d_1 from d_2, the gap width for this horizontal line is known. Then, the space-averaged gap width is calculated from the arithmetic mean of all measured gap widths for each horizontal line drawn. In the data processing procedure, the camera sends the instantaneous images to the image acquisition software at 30 frames per second. In order to measure the space-averaged gap width throughout the test, this operation requires a FOR loop in the LabVIEW code for each image. All the measurements are first made in pixels, and then converted into millimeters using a calibration taken after camera adjustment.

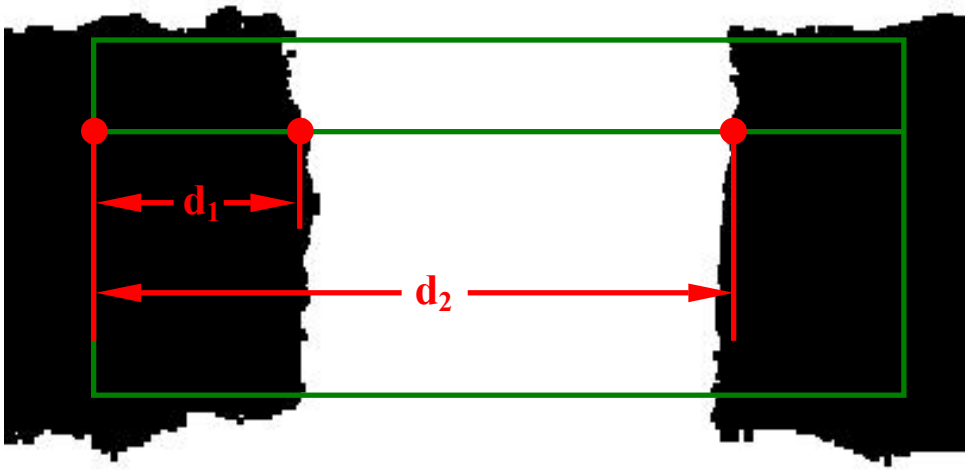

Figure 3.18 Gap width measurement.

3.2.2.5.3 Third Step of Image Analysis

The last step is the gap width control, using a comparative loop between the measured gap width (step 2) and the user specified gap width. A CASE structure is used in the LabVIEW code. If the measured space-averaged gap width is less than the user specified value then the software sends no trigger signal to the image acquisition card for activating the high-speed feeding control circuit. If the measured space-averaged gap width is greater than the user specified value then the software sends a trigger signal to the image acquisition card to activate the high-speed feeding control circuit. Then the image acquisition card sends out a TTL signal to a relay box. This triggers a relay to supply a 5-volt signal to the high-speed motor control circuit to switch on the feeding action. Otherwise, the base speed is utilized corresponding to a 0-volt signal output from the computer. Since the gap width control software is written in a loop, this process is ongoing throughout the combustion test switching the high-speed motor feeding control circuit on and off.

3.2.2.6 Motor Feed Control System

Essentially, the linear drive system has two speeds, a base speed and a high speed. Single strand testing was conducted to measure the burn rate for JA2 propellant at various pressures. These data were used to set the base speed for the two motor drives. The base speed was set slightly lower than the burn rate of a single strand allowing the burning surfaces to travel outward away from each other. The high speed is set at a level greater than the single strand burn rate in order to compensate for higher burn rates encountered during the dual-strand combustion situation. Using the comparative logic in the control software, the stepper motor's high-speed control circuit turns on and off accelerating and decelerating the propellant strands (shown in Figure 3.19), to maintain a constant space-averaged gap width.

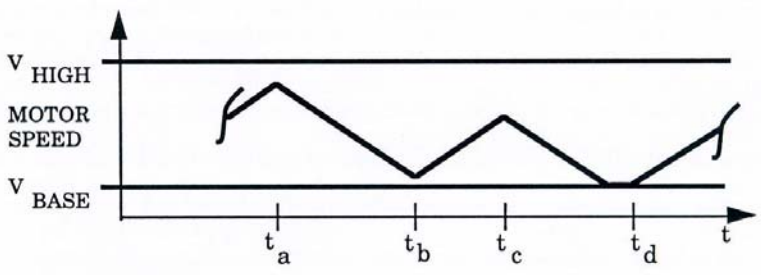

Figure 3.19 Instantaneous motor feed rate bounded by the base and high-speed limits during a test run.[2]

In Figure 3.19, at times t_a and t_c the high-speed feed circuit is switched off. At times t_b and t_d the high-speed feed circuit is switched on. The propellant strands initially start at the base-speed feeding rate. Once the average gap width measured is greater than the gap width specified, a signal is sent to the motor control to turn the high-speed feeding circuit on for both motors. When the gap width reaches the desired value, the high-speed feeding circuit is turned off for both motors. This process is continued throughout the testing period.

3.3 Experimental Test Procedure

Due to the complexity of this experimental setup many steps must be taken to ensure a quality reproducible test. There is sample preparation, optical set up, video set up, control software set up, purge system set up, and data acquisition set up. All of these steps must be repeated in a likewise manner for every test.

3.3.1 Sample Preparation

The JA2 propellant grains are manufactured in 250-mm lengths. The linear ball screw and propellant holders have a maximum travel of about 65 mm. Therefore, the propellant grains are cut into 5 pieces, about 50 mm in length. The JA2 propellant strands are then painted with a flame inhibitor. This is in addition to the nitrogen purge gas flow along the sample length to avoid any flame spreading along their lateral surfaces. For achieving more uniform ignition over the two propellant strands, a thin disc of NOSOL363 propellant is used to ignite the JA2 strands at their opposing interface. A thin disk, 2.5 mm or thinner, is cut from a longer piece of NOSOL363. This disk is then punctured through the annular surface with a thin needle and a 30-gauge nickel-chromium (ni-chrome) wire is threaded through. This assembly is then glued to the end of half of the JA2 test samples using acetone to soften the rubber-like material of the two propellants shown in Figure 3.20.

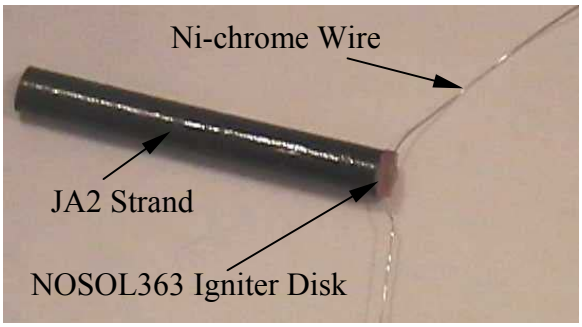

Figure 3.20 Final JA2 test sample.

When preparing to run a test two strands are selected, one with the NOSOL363 and one without. The JA2 strands are each measured for length and diameter, and the NOSOL363 disk is measured for thickness. This is then recorded on the test data sheet.

3.3.2 Test Rig Assembly

Once the JA2 strands are prepared and measured they can be inserted into the test rig. Both sides of the chamber open as previously described with the flangeless couplings. On the right side of the chamber the JA2 without the igniter is installed by feeding the linear drives out about halfway, and then pressing the JA2 strand onto the needle on the end of the propellant holder. The motor drive is then reversed so the propellant is only sticking out about 5-10 mm. The left side is installed likewise, however, after drawing the propellant back through the propellant guide the igniter leads are connected as seen in Figure 3.21. After both strands are installed they are fed in towards each other until they touch. Then, they must be checked for alignment in both the top and side axes to guarantee the surface of the two propellant strands will burn evenly. Finally the high-pressure vessel is resealed.

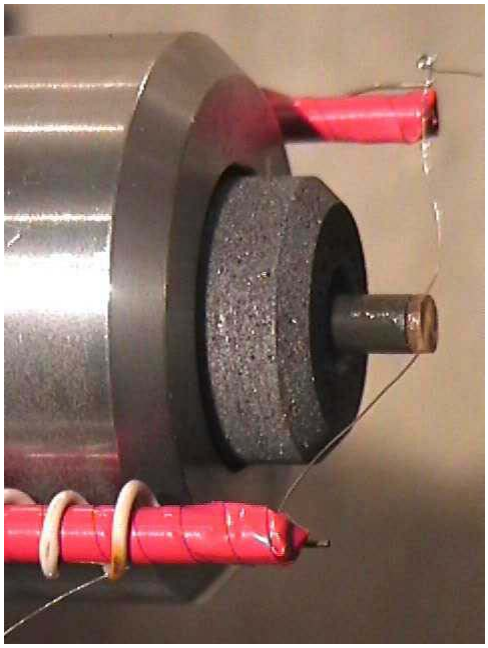

Figure 3.21 JA2 propellant strand with igniter installed in test rig.

3.3.3 Optical Setup Procedure

To ensure the control feedback loop receives a good image the optics and laser must be in good alignment with the center combustion chamber and the black-and-white CCD camera. First, the expanding and collimating lenses need to be placed at the correct distance apart from each other. Next, the center of the laser and the center of the lenses need to be in line. Once this is accomplished the expanded beam is reflected down through the combustion chamber and then to the front of the CCD camera. Finally, the image is zoomed and focused as close as possible to the two propellant surfaces.

3.3.4 Video Recording Setup Procedure

Since the DEWSB has four windows total and only two are used by the control feedback loop, the others are used to capture a color image. Both color and black-and-white cameras are connected to a video setup consisting of a TV, VCR, and key generator. The key generator puts

text on the video screen. It also provides a stopwatch to record the testing time. For each test the color and black-and-white images are recorded with the date, stopwatch time, project name, test number, and chamber pressure. The videos are used after the test to evaluate whether the test was good or not, (i.e. no side burning, constant gap width, flat burning surface, etc.), and for data reduction purposes.

3.3.5 Control Software Setup Procedure

Once the JA2 propellant is installed, the test rig is sealed, and the optics are aligned, the control software can be configured. The control software consists of two programs written in LabVIEW. The first program is used to select the region of interest that the second program uses to calculate the gap width between the two propellant strands and provide feedback to the motor control.

3.3.5.1 Region of Interest Program

When the first program is started a window appears inside of the main program window. This window contains the post-processed black-and-white image. The box in the center of the program window controls the threshold level for the image. Once the threshold is set, the region of interest is controlled by inputs for the left, right, top, and bottom boundaries. LabVIEW imaging software uses pixels for measurements. Therefore, the numbers input in the controls are in pixels. The top left corner of the image window is considered to be the coordinate 0, 0 and the bottom right corner is 640, 480 since the resolution of the image is 640x480. The top and left inputs are the boundaries of the top and left, and the bottom and right inputs are the boundaries of the bottom right. After these are input a green box appears in the image window as the region of interest. For example in Figure 3.22 the region of interest is bounded horizontally by the boundaries at 15 and 625 pixels, and vertically by the boundaries at 150 and 310 pixels. The

reading of number of lines is an output corresponding to the difference between the top and bottom boundary lines.

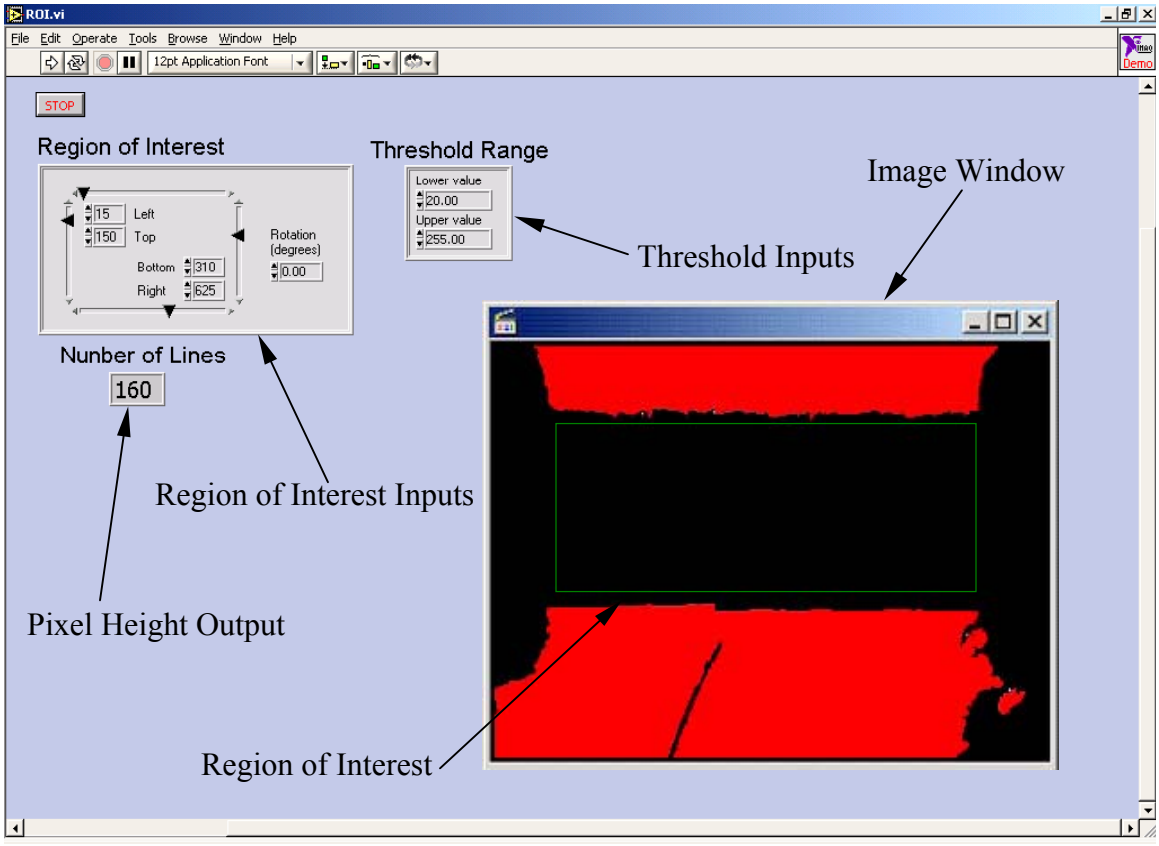

Figure 3.22 LabVIEW program used to find the region of interest.

After a suitable region of interest is found, suitable meaning a region of interest that will encompass the burning surfaces of the propellant strands and the gap width between them, the boundaries can then be input into the gap width measuring and feedback program.

3.3.5.2 Gap Width Measurement and Control Feedback Program

The same inputs used for the threshold and boundary lines need to be input in the second program. However, the bottom boundary line is replaced with the number of lines output from the first program. This tells the second program how many lines to draw across the region of interest to measure the gap width. There are also a few more inputs for the second program.

The first input to the second program is the names and locations for the output files. The second program records the gap width over the time of the test, as well as an audio video interleave or more commonly known as an AVI file, (video clip), of the post processed image seen in Figure 3.23. These files are saved for data reduction and post processing of the tests.

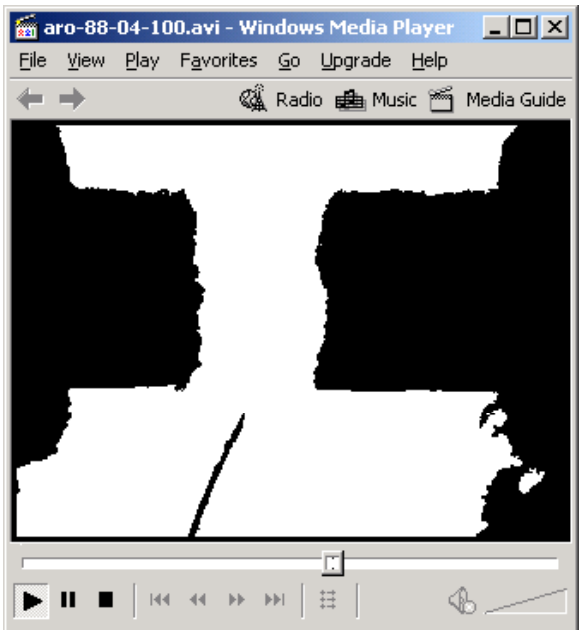

Figure 3.23 AVI file of two propellant strands burning after image processing.

The second input, is the desired gap width. This is the user specified gap width that the program and motor drives will try to hold constant. Finally, the conversion factor to convert pixels to millimeters needs to be input. This is needed because LabVIEW computes in pixels, so the gap width measured needs to be converted to millimeters to be able to compare it to the user specified gap width. The conversion factor comes from another LabVIEW package called Vision Builder. In Vision Builder the minimum and maximum propellant diameter is measured in pixels and then averaged. Then the actual measurement of the propellant diameter is measured in millimeters and divided by the average measurement in pixels. This number is the

conversion factor in mm per pixels. Figure 3.24 is the LabVIEW control window for controlling the gap width.

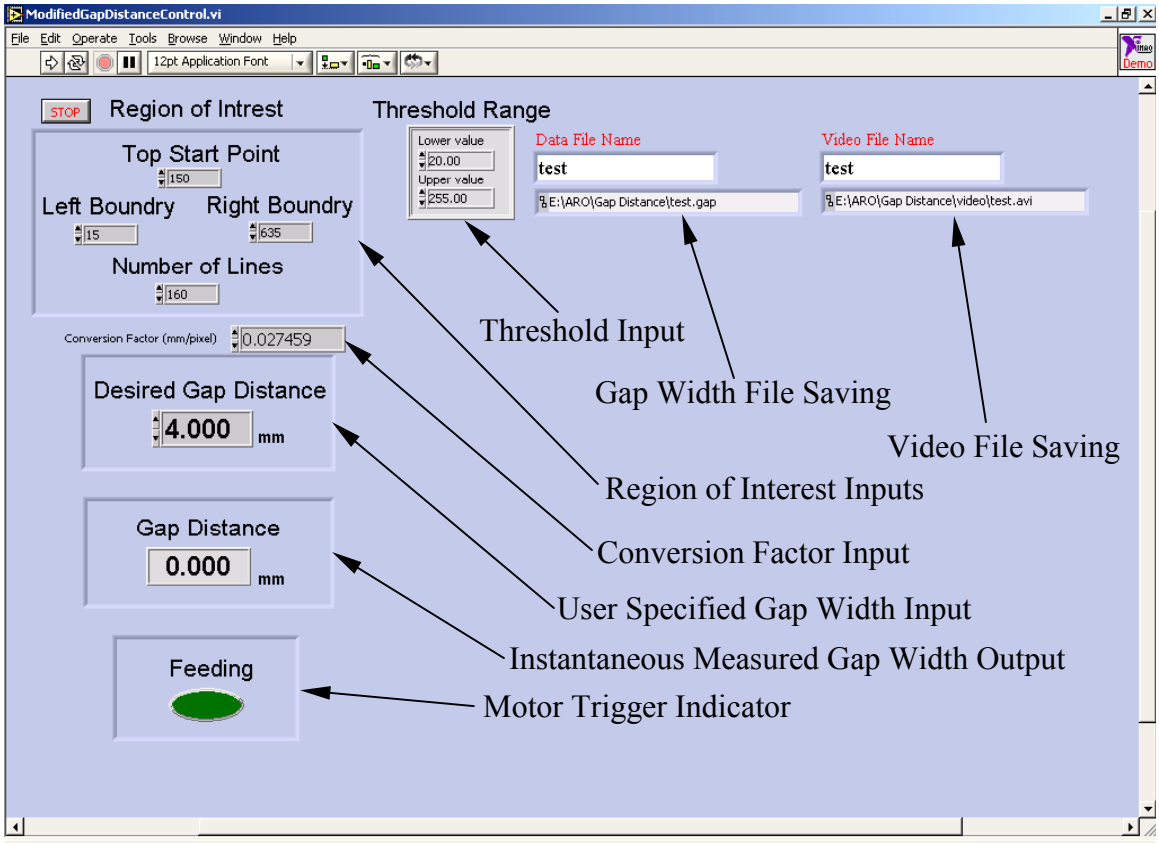

Figure 3.24 Gap width control LabVIEW program.

3.3.6 Nitrogen Purge System Setup Procedure

The next step in preparing to run a test in the DEWSB is to get the purge flow system ready. First, the pressure in the reservoir must be about two times higher than the operating pressure for the test. The reservoir for the main chamber is made of five nitrogen bottles connected to a manifold, and the reservoir for the window purge is made of two nitrogen bottles connected to a manifold. Second, the hand valves controlling the flow to each side of the pressure chamber need to be set. Next, the needle valve for the window purge needs to be set. Once these are set the purge into the system is ready.

The next step in preparing the purge flow system is to set the hand valve inline with the solenoid valve. After this, the upper and lower limit for the solenoid valve must be set in the control computer. The upper limit and lower limit pressures are input into a Qbasic program used for controlling the chamber pressure. The control computer has a small data acquisition board that reads the voltage from a pressure transducer and outputs a signal to a solid-state relay to trigger the solenoid open or closed. The data acquisition board is a Dataq DI-194 4-channel data acquisition module, and the pressure transducer is a Setra pressure transducer with a range from 0-3000 psig. Finally, the pressure in the chamber is adjusted during the test by opening the regulators to the reservoir manifolds and by opening and closing the remote valve via the control computer to regulate the exhaust flow out of the chamber.

3.3.7 Data Acquisition System Setup Procedure

During a test run, the data acquisition system records the outputs from the two linear potentiometers, the pressure transducer, and the feeding motor control signal. These data are recorded on a LabVIEW data acquisition system at a frequency of 1000 Hz. All signals are recorded as voltages and then converted by a calibration curve for each diagnostic instrument. Figure 3.25 shows the channel set up for the different diagnostics connected to the data acquisition system.

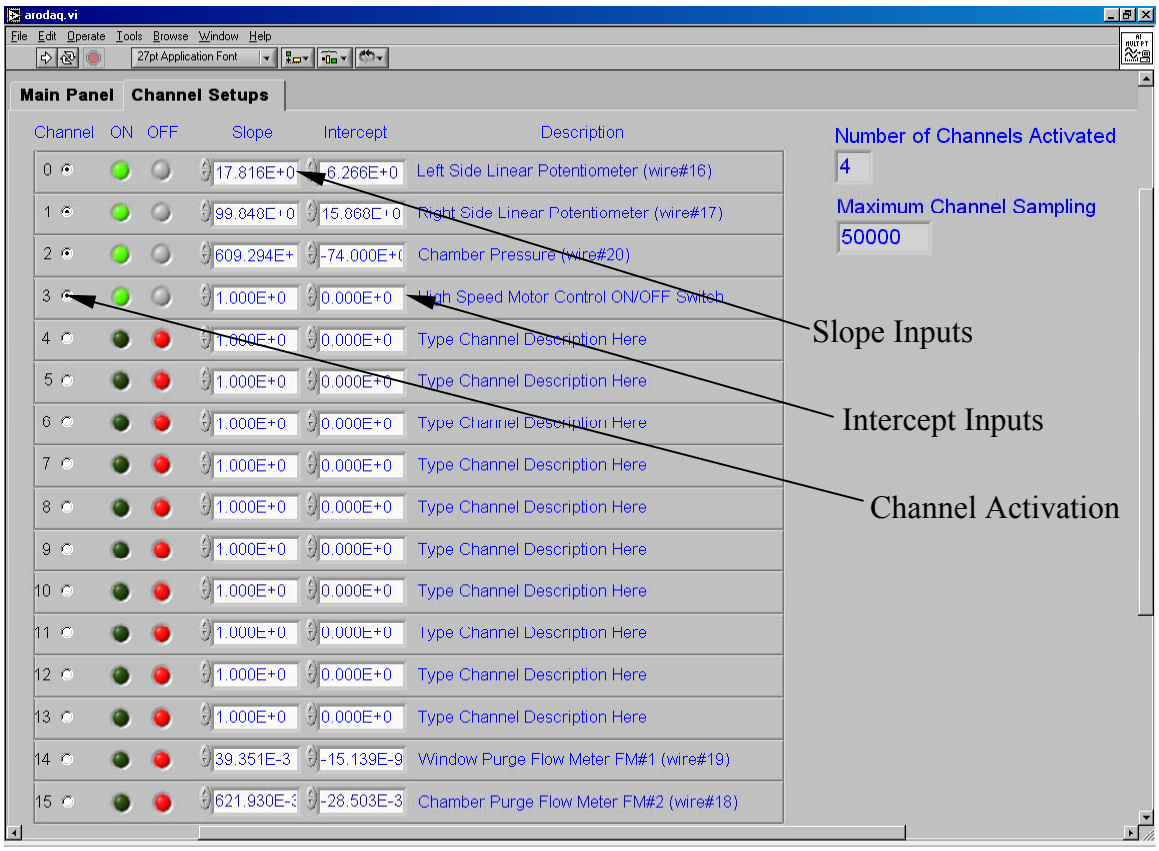

Figure 3.25 LabVIEW data acquisition channel set up.

Figure 3.26 is the front panel for the data acquisition system. The program has inputs for the saved file name, sweep time, and sampling rate. The data starts recording once the program is running then triggered. It acquires data for all activated channels for the duration of the sweep time. Once the test is complete the data is displayed in graphical form in the plot window.

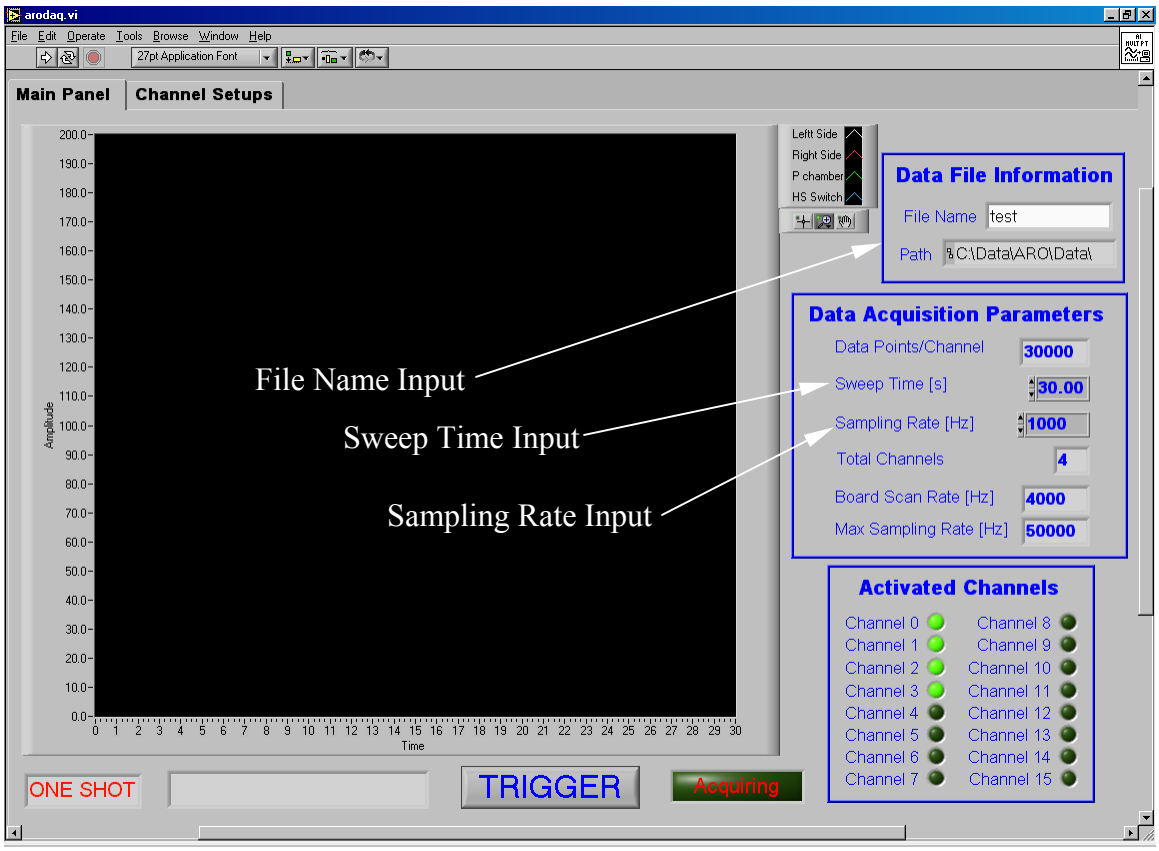

Figure 3.26 LabVIEW data acquisition front panel.

CHAPTER 4 Results and Observations

4.1 Experimental Test Apparatus Verification

To keep a constant gap width between the burning strands of propellant, the high-speed switch needs to be triggered on or off as the gap width changes. Figure 4.1 shows the response time of the online control system switching as the gap width changes. When the measured gap width is larger than the desired gap width, the software triggers the high-speed switch on. As the gap width is reduced due to the acceleration of the propellant strands, the measured gap width falls below the desired gap width and the software triggers the high-speed switch off.

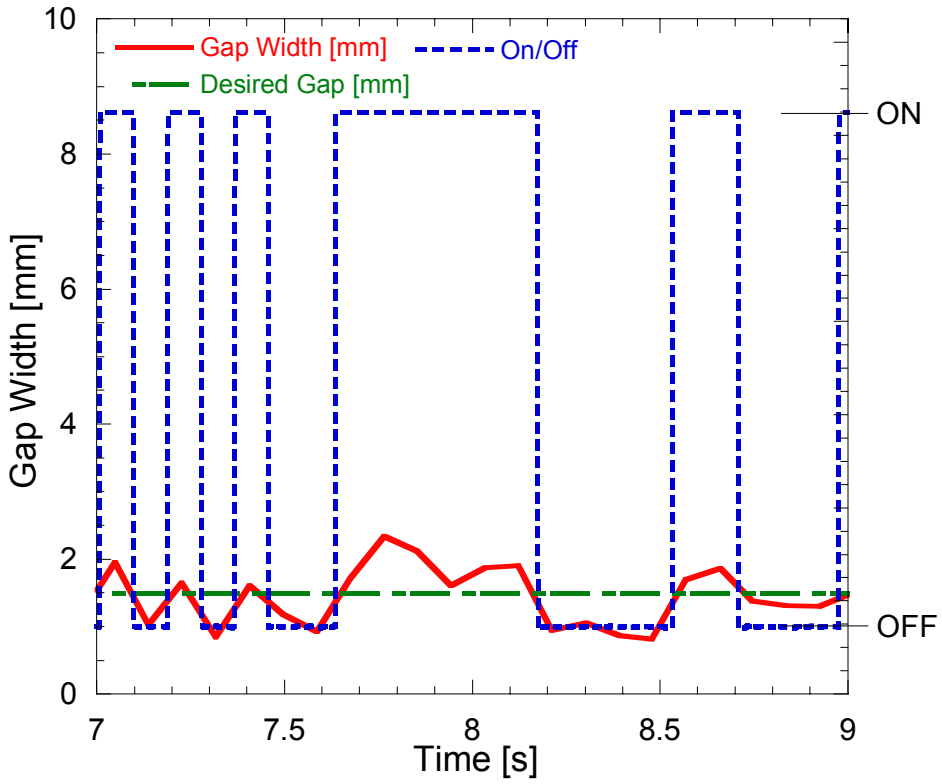

Figure 4.1 High-speed switching according to the measured instantaneous gap width.

The response time of the motors needs to be relatively fast in order to maintain a constant gap. The motors must be able to switch from the base speed to the high speed and back to the

base speed as needed. Figure 4.2 shows the velocity of the motors as the high speed is switched on and off. When the high speed is switched on the motors accelerate the propellant to the high-speed setting. When the high speed is switched off the motors decelerate the propellant to the base-speed setting.

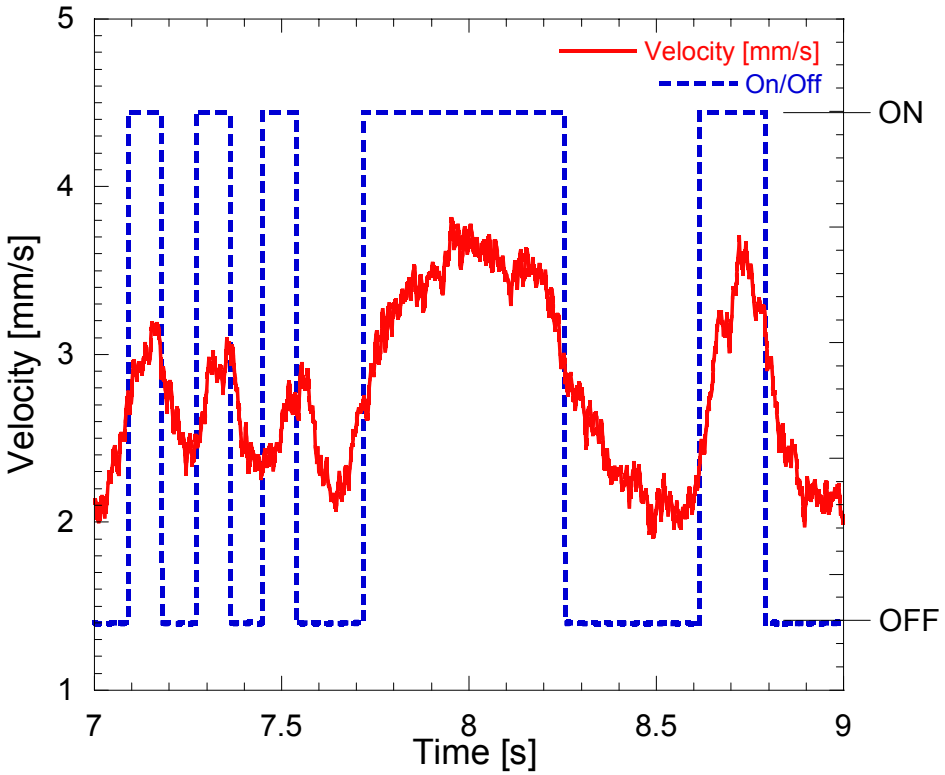

Figure 4.2 Motor velocity response to high speed switching.

To determine whether the software was measuring the correct average gap width, the data output was compared to a measurement of the gap width from the actual video image. The image input to the software is from a top view, where the image input to the colored video is from a side view. Analyzing both views gives a more complete picture of the burning surface and the gap width between the burning propellant surfaces. From review of the video image, a time frame was chosen after the onset of ignition when the burning propellant surfaces seemed to

be mostly uniform and the gap width was held constant. Between these times a measurement of the gap width was taken. This gap width compared very closely to the gap width measured by the software as seen in Figure 4.3.

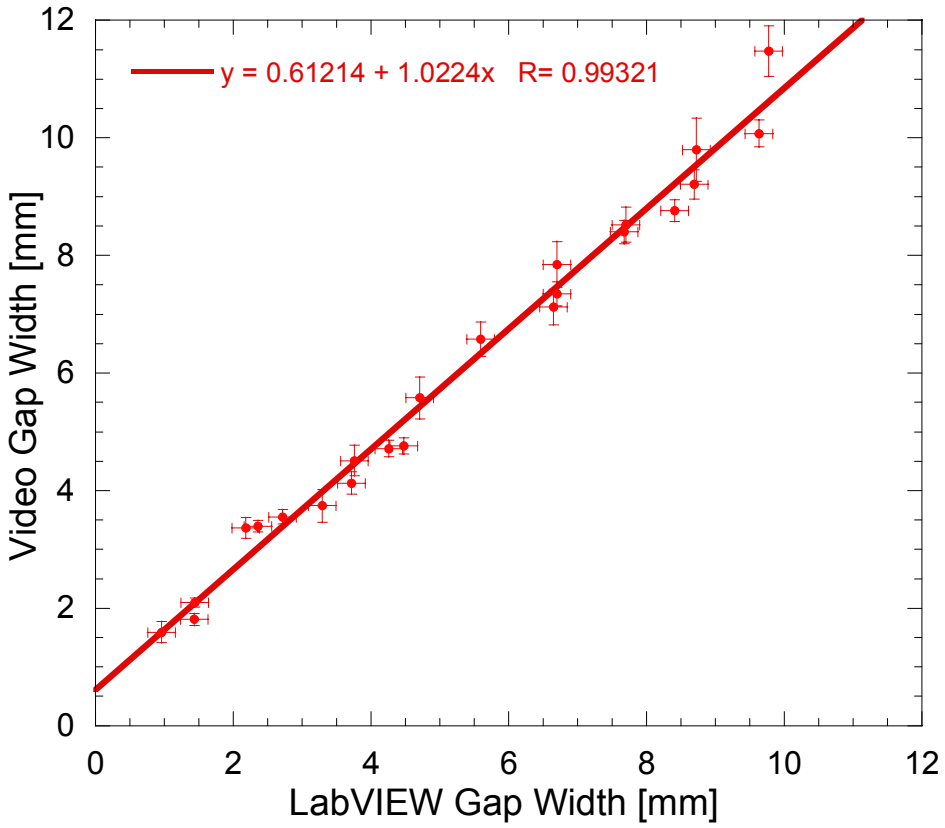

Figure 4.3 Comparison of gap width measured by LabVIEW software and video analysis.

4.2 Recorded Images

The DWESB has four windows evenly separated 90º from each other. The black-and-white CCD camera uses the top and bottom windows. The side windows are used to record a color image with a color CCD camera. Figure 4.4 and Figure 4.5 are color images taken from the front side of the combustion chamber.

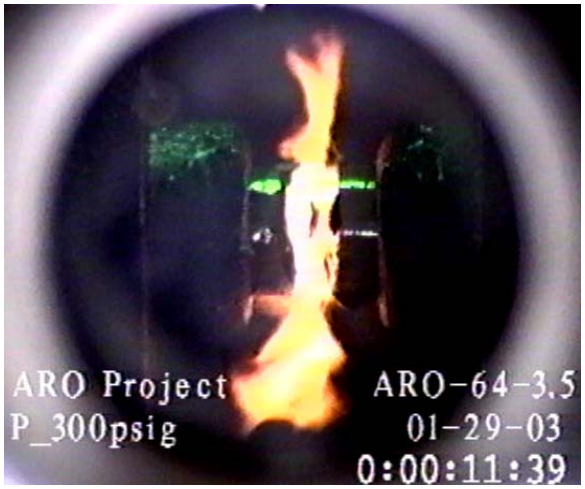

Figure 4.4 Color image of JA2 propellant burning at a P = 2.07 MPa with an instantaneous spatial-averaged gap width of 1.56 mm.

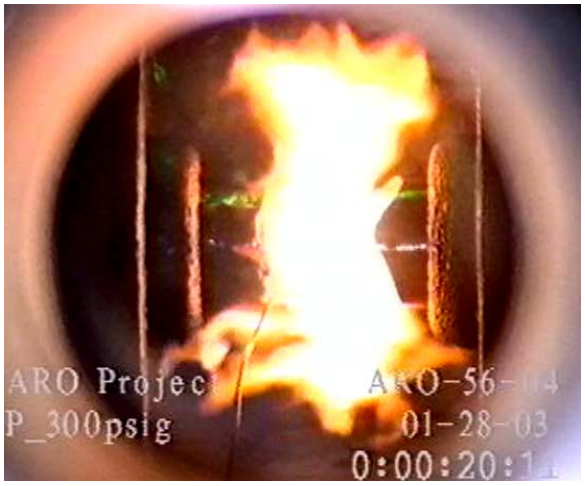

Figure 4.5 Color image of JA2 propellant burning at a P = 2.07 MPa with an instantaneous spatial-averaged gap width of 3.30 mm.

Both images were taken at a pressure of 2.07 MPa. The first has an instantaneous spatial-averaged gap width of 1.56 mm, and the second has an instantaneous spatial-averaged gap width

of 3.30 mm. Figure 4.6 and Figure 4.7 are raw images recorded by the black-and-white CCD camera from the bottom window of the combustion chamber of the same two tests.

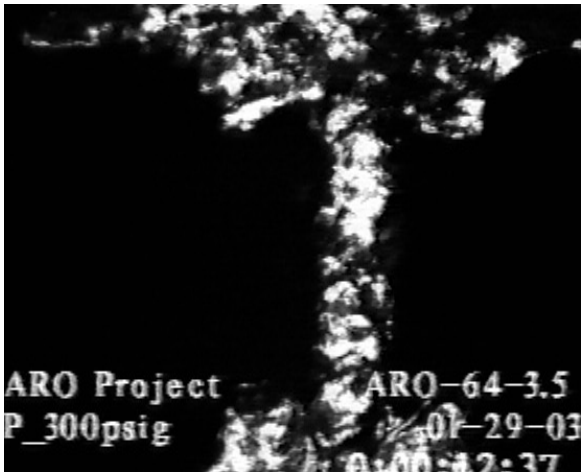

Figure 4.6 Black-and-white image of JA2 propellant burning at a P = 2.07 MPa with an instantaneous spatial-averaged gap width of 1.56 mm.

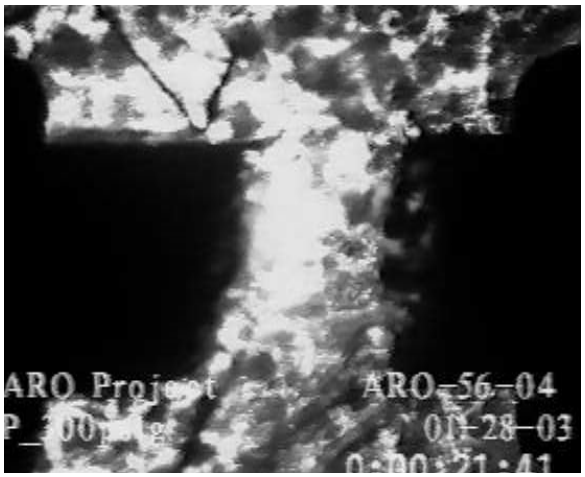

Figure 4.7 Black-and-white image of JA2 propellant burning at a P = 2.07 MPa with an instantaneous spatial-averaged gap width of 3.30 mm.

After the LabVIEW control program processes the raw black-and-white image it turns into the contrasting images seen in Figure 4.8 and Figure 4.9. These are the images where LabVIEW measures the gap width.

Figure 4.8 LabVIEW processed image of JA2 propellant burning at a P = 2.07 MPa with an instantaneous spatial-averaged gap width of 1.56 mm

Figure 4.9 LabVIEW processed image of JA2 propellant burning at a P = 2.07 MPa with an instantaneous spatial-averaged gap width of 3.30 mm

4.3 Burning Surface Observations

It is interesting to note that the burning surfaces of the opposing strands are not very uniform and smooth when the gap width is reduced below about 2 mm. There are a few reasons for this. In most of the narrow gap width burning tests, the burning surfaces are not truly planar; instead the boundaries of the gap space are continuously varying with respect to time, while keeping the average gap width constant. Secondly, there are carbonaceous residues generated with non-uniform distribution at the propellant burning surface. This non-uniformity causes the local surface regression rate to be non-uniform; hence producing non-uniform streams of combustion products flowing against the opposing propellant product stream. The flow turning phenomena in the narrow gap zone can be seen clearly in Figure 4.10. Even though the Reynolds number of each of the opposing stream of combustion product from the burning propellant surface is below 1000, this combined stream after the flow turning has to exit from the narrow gap zone in the radial direction. There is a significant amount of flame stretching effect, which could cause the propellant flame to be weaker or stronger at different spatial locations.[17] As shown by Bray[17] under strong flow conditions the flame between two opposing jets can have a wrinkled contour. The propellant flame can also be affected by the turbulence eddies generated in the gap width zone.

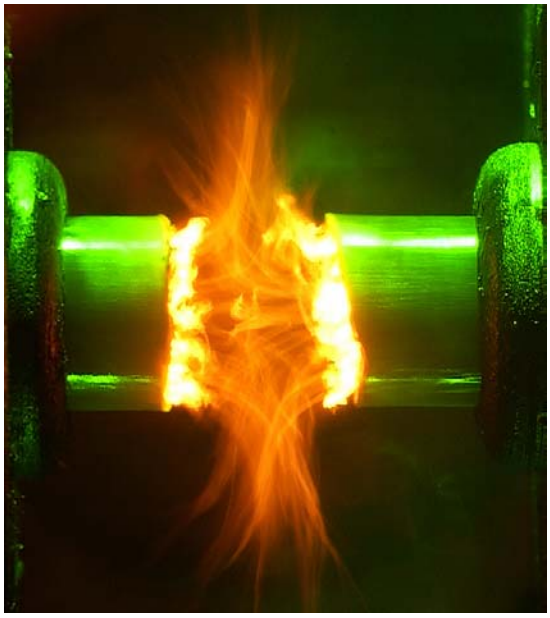

Figure 4.10 Flow turning and carbonaceous residues ejection from the burning surface of two opposing propellant strands.

At close gap widths these “flakes” could be momentarily trapped between the two surfaces and cause the propellant to burn back in those spots producing the uneven burning surface. The intensity of the flame in the gap space is also non-uniform. The non-uniformity burning inside the gap width zone causes the burning surfaces to change continuously.

4.4 Test Data

As previously stated the data acquisition system records the outputs from the two linear potentiometers, the pressure transducer, and the feeding motor control signal. In addition to this, the gap width control loop records the gap width. The data reduction is a complicated process due to the fact that the confined flame may cause uneven burning surfaces of the JA2.

4.4.1 Individual Test Data Reduction

After a test is completed all raw data is plotted on the same chart and then analyzed to establish when ignition occurs. Ignition is determined by when the linear drives are first

activated. When the linear drives are activated the slope of the output from the linear potentiometers changes and this is considered to be the time for onset of ignition, t_{ign}. Figure 4.11 is linear potentiometer data for the first 10 s of a test. At the time around 5.5 s there is a slope break. This point is when the ignition of the JA2 takes place and is considered to be t_{ign}.

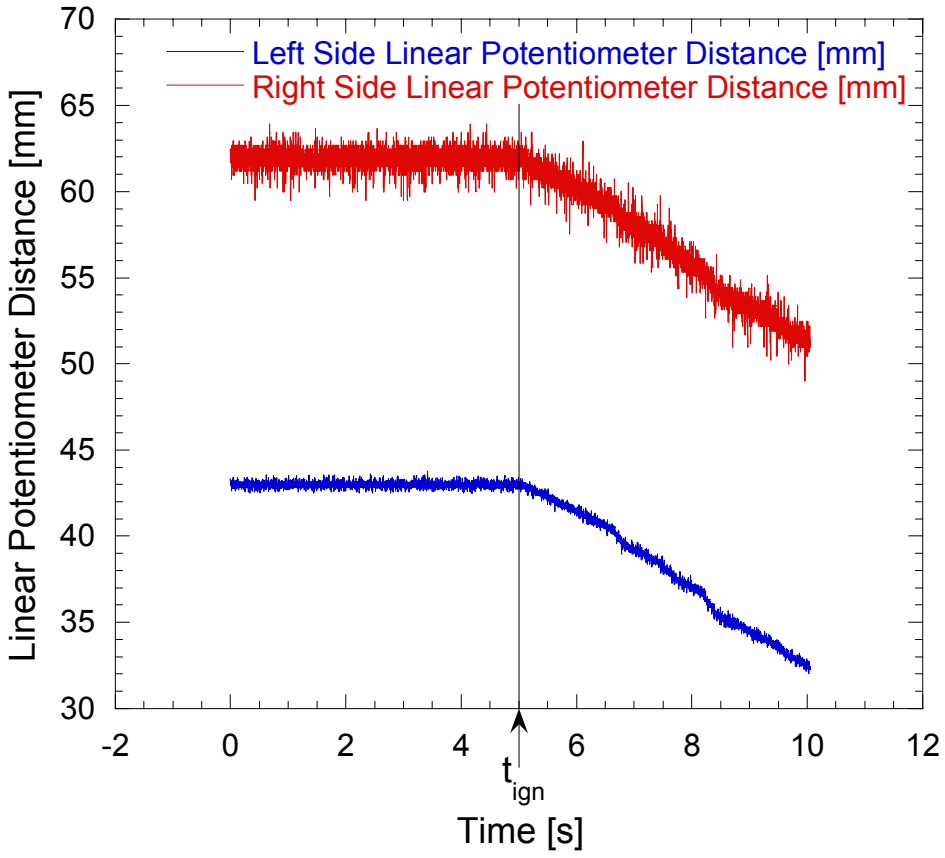

Figure 4.11 Determination of the time for onset of ignition, t_{ign}.

Once the ignition time is established, the high-speed switch and gap width data recorded are plotted with respect to time in reference to the onset of ignition treated as time zero, (i.e.; t_{ign} = 0 s). This plot is used to resolve a time range for which the time-averaged gap width is constant. The gap width originally starts at 0 mm and the high-speed switch starts at a voltage near 0 V. As the propellant burns back to the specified gap width the switch receives an input of

5 V. As previously described, this input turns the high-speed switch on and off continuously throughout the test period. The time range where the gap width is constant is considered to be between two points, t_1 and t_2, when the switch is consistently cycling.

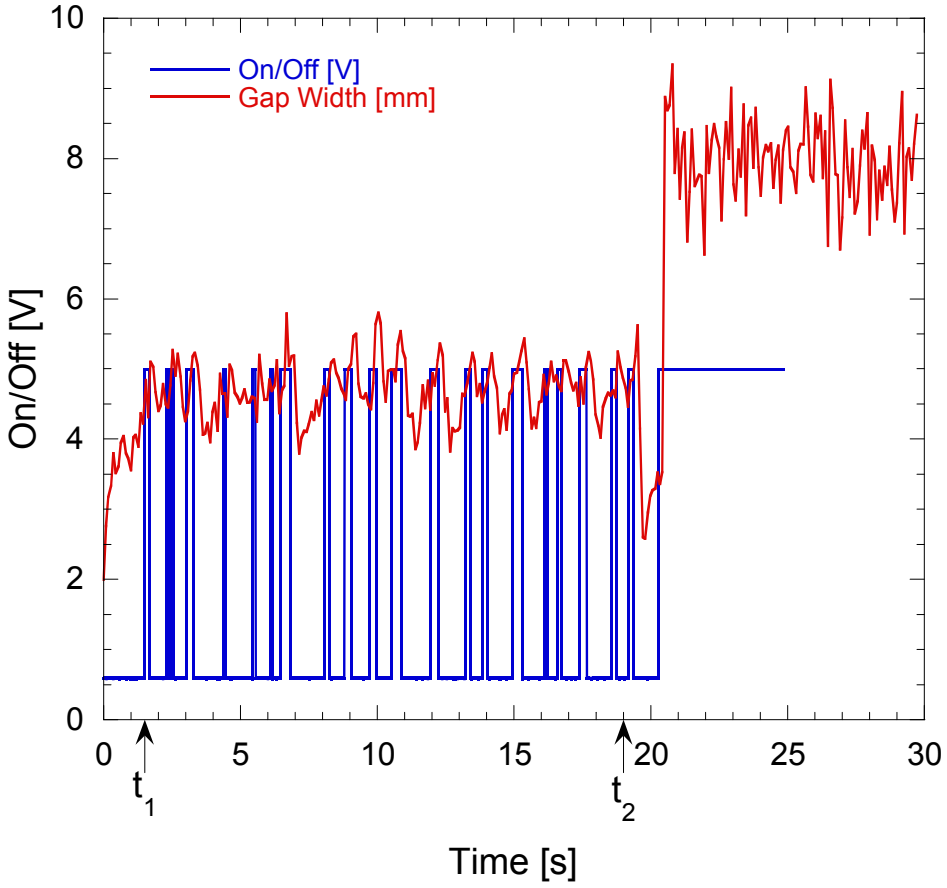

Figure 4.12 Typical trace of the instantaneous space-averaged gap width and the indicator function showing the on and off periods of the high-speed switch.

The first 1.5 seconds of the data is cropped (up to t_1) since the gap width has not reached the desired level. Similarly, the very end of the data is cropped from the point t_2, where the linear motors reach their upper limit and stop feeding the propellant allowing the strands to burn back. This is the time period in which the measured time-averaged gap width and the associated burn rate from the linear potentiometer outputs are found. Figure 4.13 is the gap width plotted

from the LabVIEW control program. The time-averaged gap width is found by fitting a linear curve to the data.

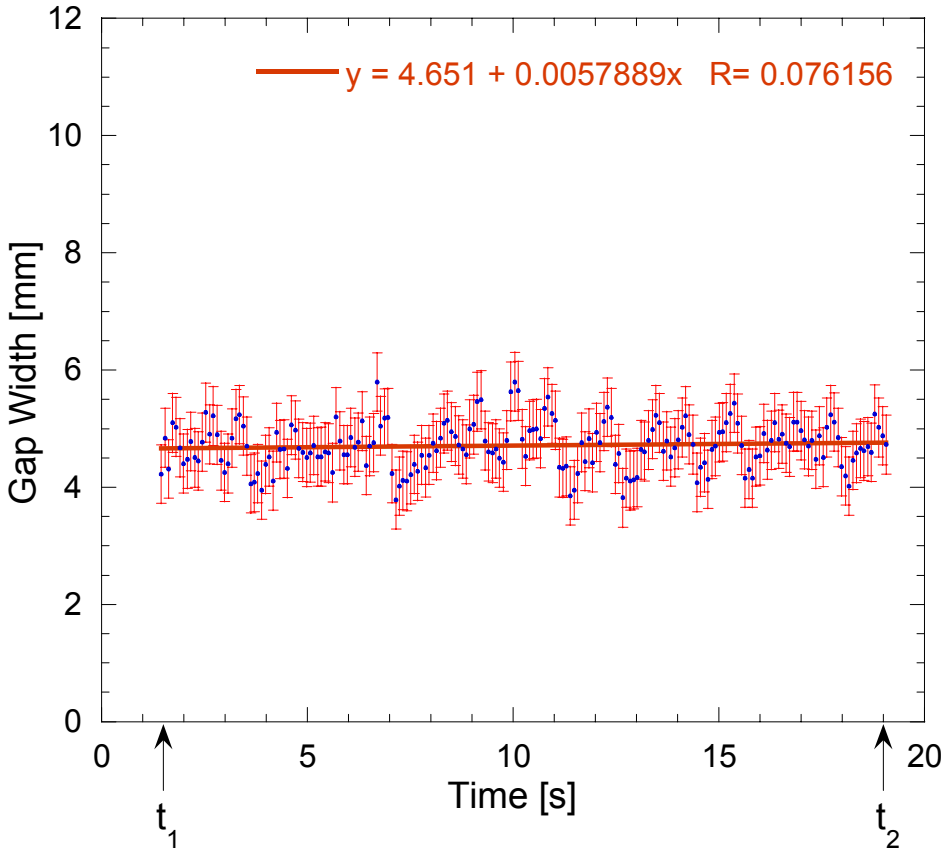

Figure 4.13 Time-and-spatial averaged gap width measured by the LabVIEW control program.

Figure 4.14 is the data from the linear drive potentiometers for the given time period. A linear curve is fit to the data and the slope of the curve is the speed of the linear drives. Since the time-averaged gap width is considered to be constant between t_1 and t_2, the propellant burning surface is deemed to be stationary. Therefore, the output from the linear drives is considered to be the burn rate of the JA2 propellant.

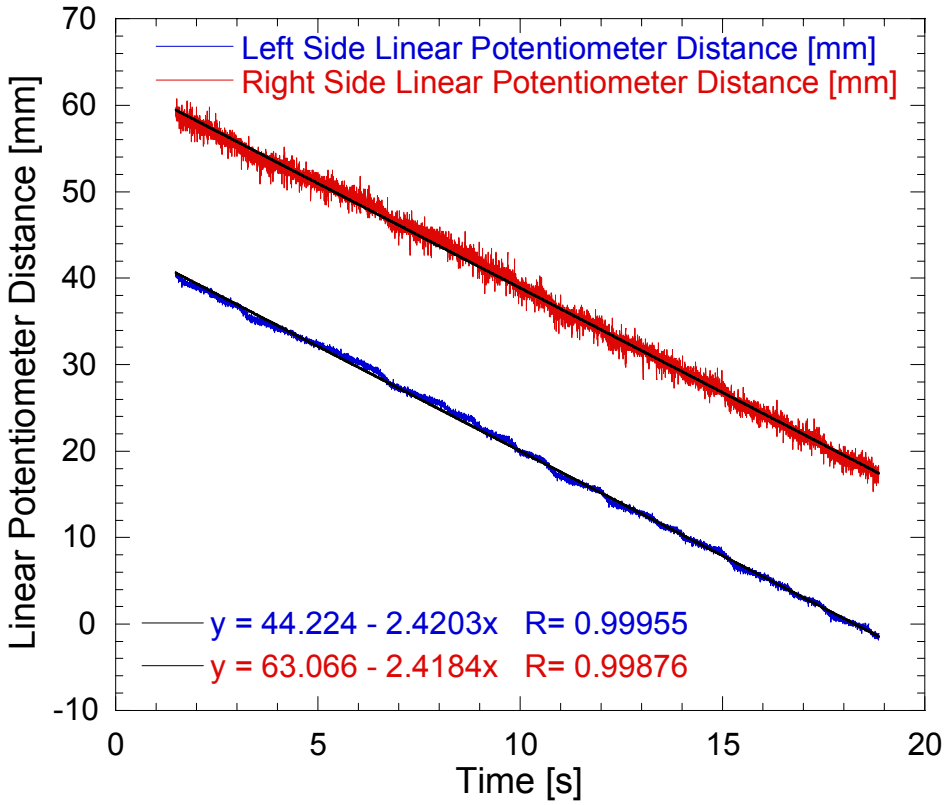

Figure 4.14 Speed of the linear drives corresponding to the regression rate of the propellant strands for the selected time period.

There are two main things to note about the data recorded. First, the left- and right-side linear potentiometer data are offset from each other. The offset between the two sides has to do with the length of the propellant holder arm. They are different lengths and therefore when calibrated, their zero point is at a different measurement. However, the two lines are parallel indicating that their average speeds are the same. Second, the data for the right-side linear potentiometer seems to be more scattered than the left-side linear potentiometer. This is due to the internal circuitry of the drive system for the linear potentiometers. The right-side linear potentiometer was damaged before the experimental test rig was first used for this particular study and was replaced. However, the original part could not be found so a suitable substitute

was used. All of the specifications were met except the resistance of the new potentiometer is ten times less than the old potentiometer. The original circuitry was designed with an amplifier for the old potentiometer and so the new potentiometer has more electrical noise than the old one. However, the signal is recorded at 1000 Hz so there is enough data to rule out any error associated with the electrical noise.

The next step in the analysis of the data is to make sure that the propellant burning surface is relatively flat. The color video is used to examine the instantaneous images of the burning propellant strands. The first step in this process is to determine when the JA2 propellant is ignited, immediately following the burn out of the NOSOL363 igniter propellant. Figure 4.15 shows a set of video images taken during the start up process.

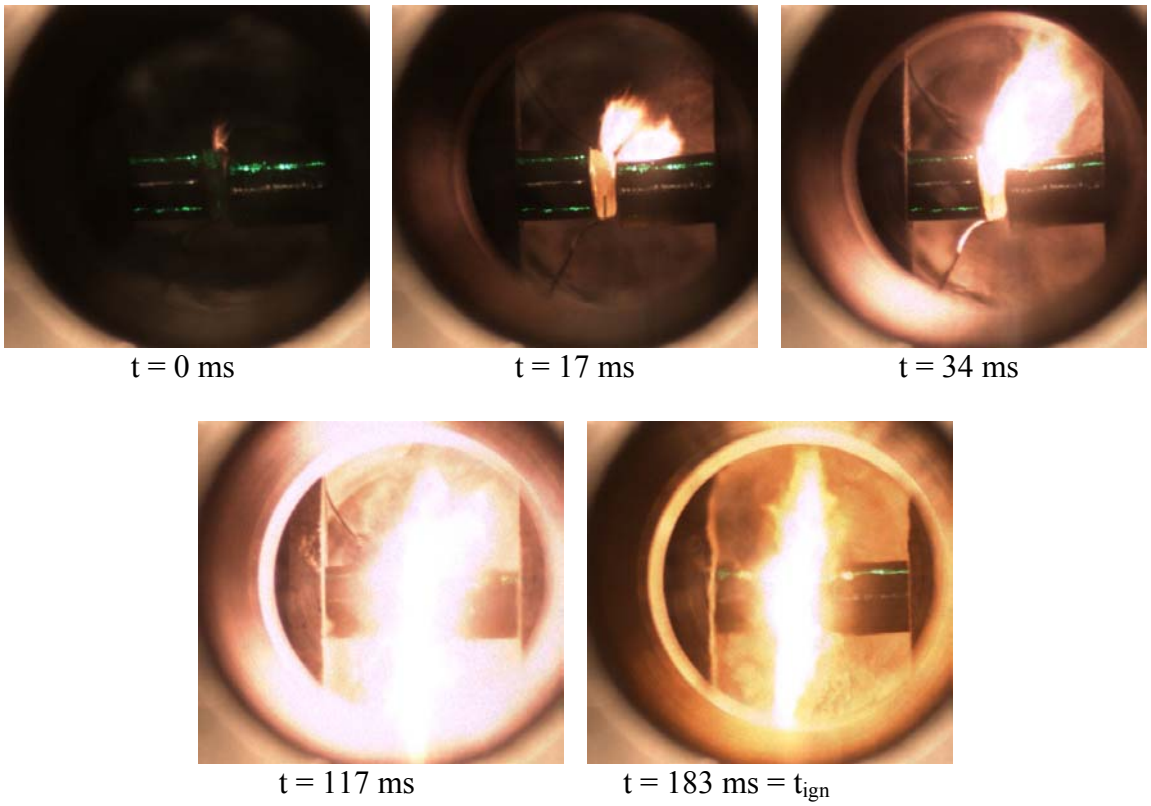

Figure 4.15 Ignition of JA2 propellant by means of NOSOL363 igniter propellant.

At t = 0, an electric current is sent through the NOSOL363 propellant disk. Through the next 100 or more milliseconds the NOSOL363 is burned igniting the JA2 strands, until t = 183 ms and the JA2 is completely ignited on the top surface. This time is used to define the onset of ignition, t_{ign}. The video is then viewed for the subsequent time period when the gap width is constant. The gap width is measured on the video screen with a metric scale. Since this measurement is larger than the actual gap width due to the zooming of the camera lens it needs to be scaled accordingly. A measurement of the propellant diameter is taken from the video screen. The correction factor is determined from the actual propellant diameter. Finally, the screen measurement of the time-averaged gap width is multiplied by the correction factor to find the actual gap width. The actual gap width is compared to the time-averaged gap width from the LabVIEW output (seen previously in Figure 4.3), for the test period. The result of this comparison between these two types of measurements is quite linear; the line is very close to the 45-degree line on Figure 4.3. The departure from the 45-degree line is due to the different viewing angle at 90^o apart.

After looking at the color video a new time period is determined when the time-averaged gap width is constant. This time period falls within the old time period (based upon the LabVIEW system) and is selected as the test period when the propellant burning surfaces are relatively flat on all axes. Thus, the linear drive speed needs to be evaluated for the selected test period. Figure 4.16 shows the speeds of the linear drives as the slope of the time variation of the averaged gap width for the selected test period. Now that the speed for each propellant strand drive is found, they are averaged together to give the calculated burning rate of the propellant strands maintained at the time-averaged gap width.

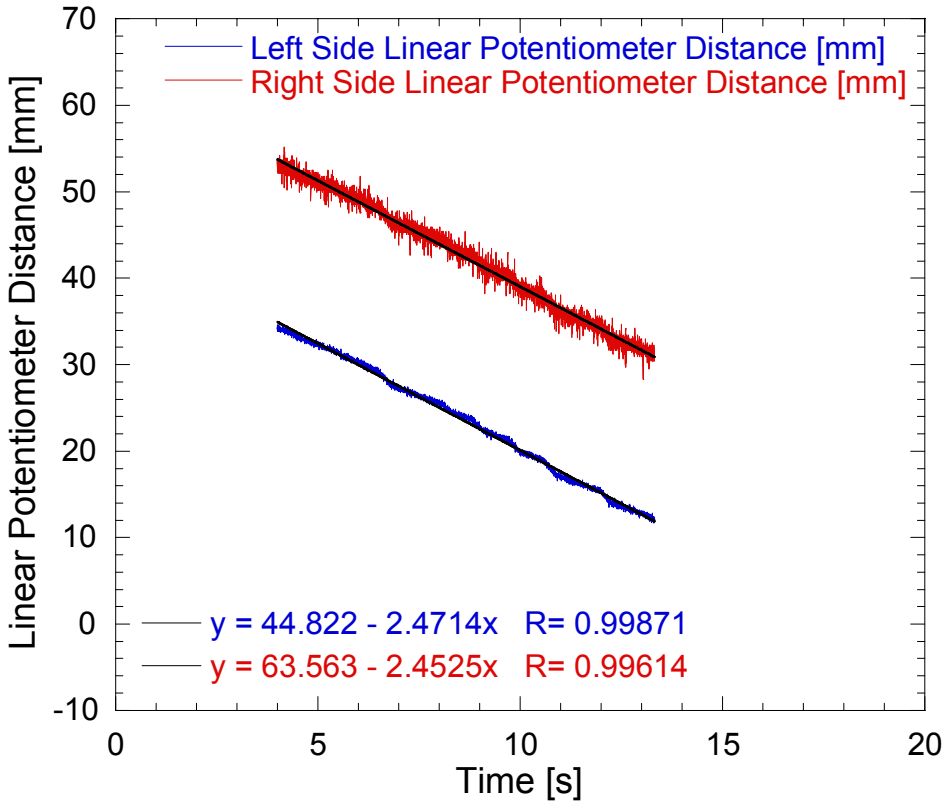

Figure 4.16 Speed of the linear drives corresponding to the slope of the time variation of the averaged gap width for the selected test period.

4.4.2 Compiled Burning Rate and Gap Width Test Data

Multiple tests were conducted for a wide range of gap widths at chamber pressures of 0.69, 2.07, and 3.45 MPa (100, 300, and 500 psia) . There are more test data for the lower pressures due to the fact that there is less combustion product gas being produced, and therefore the gap width can be more accurately measured. Also, at the lower pressures the dual propellant burning surfaces are more uniform. Figure 4.17, Figure 4.18, and Figure 4.19, are plots of the burn rates of dual strands of JA2 burning with different gap widths.

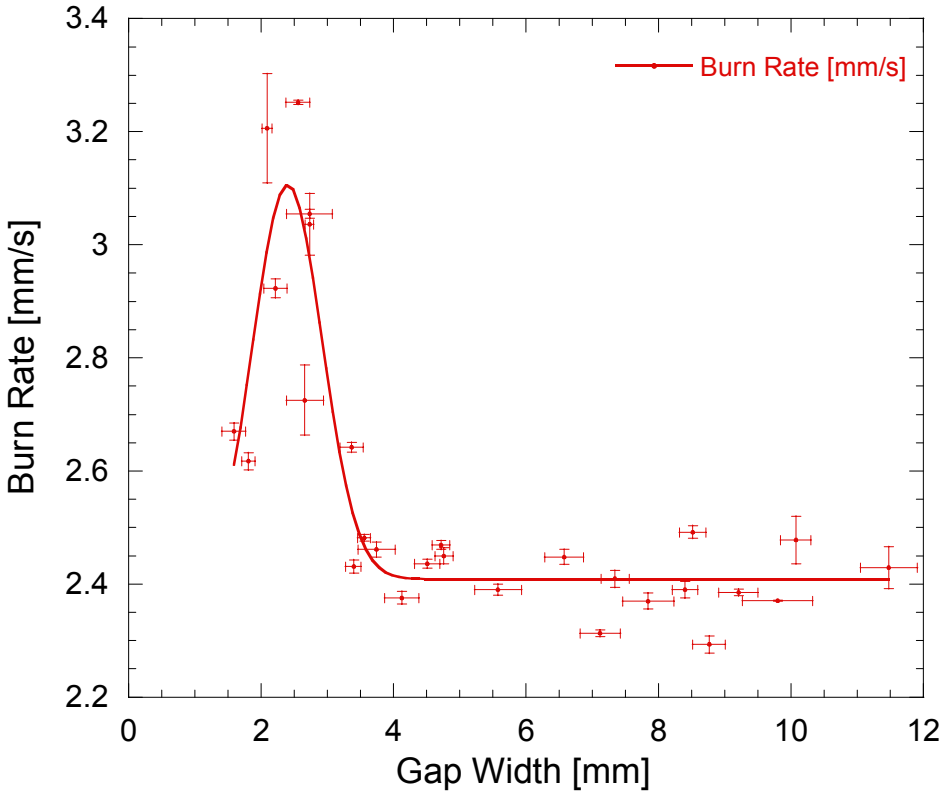

Figure 4.17 JA2 propellant burning rate for a range of gap widths at 0.69 MPa.

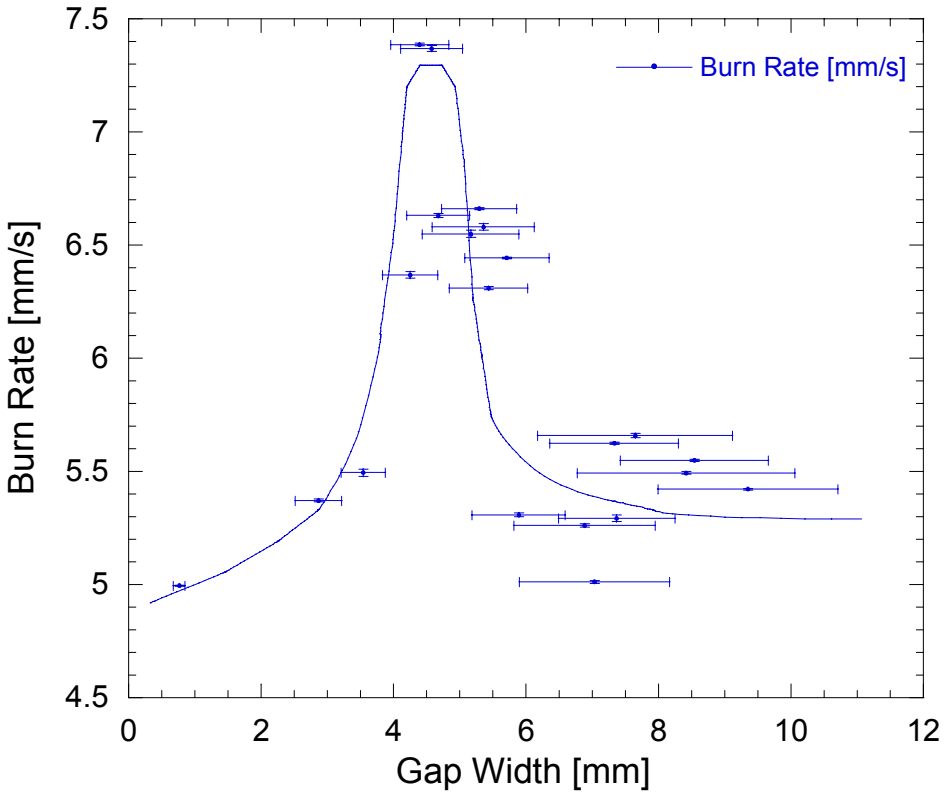

Figure 4.18 JA2 propellant burning rate for a range of gap widths at 2.07 MPa.

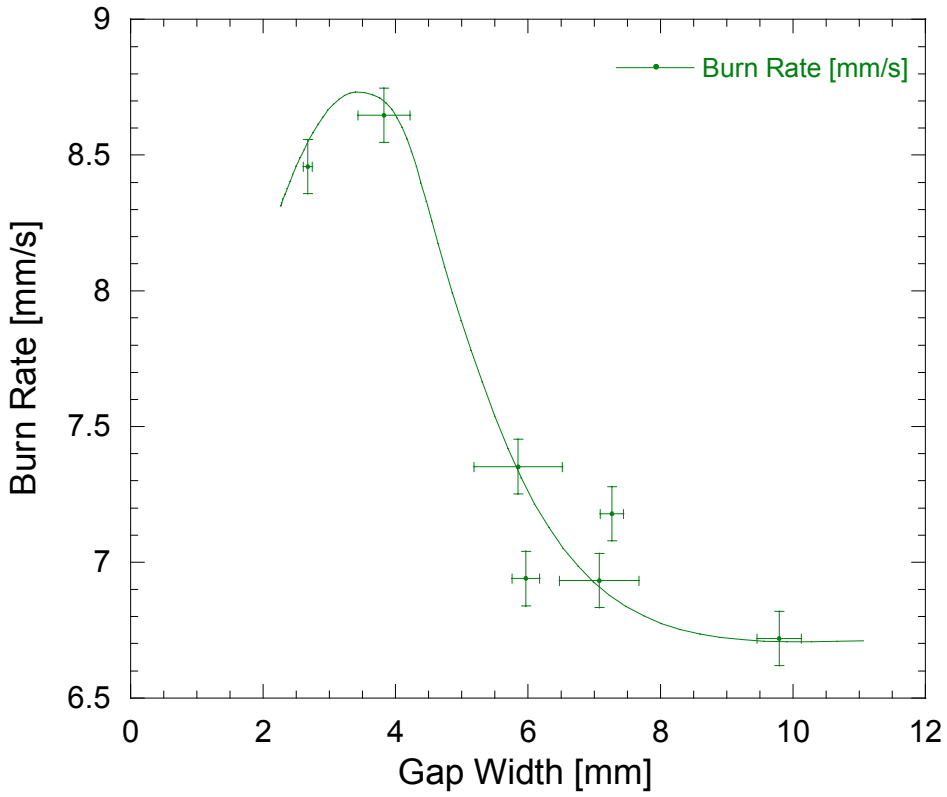

Figure 4.19 JA2 propellant burning rate for a range of gap widths at 3.45 MPa.

4.5 Data Correlation

Since a peak burning rate exists for each pressure tested, a curve fit function can be developed to represent the variation of the burning rate as a function of the gap width at a specific pressure. To correlate the data for dual propellant strand burning, the data for single propellant strand burning is also used as the asymptotic value at large gap widths. Specifically, the single strand burn rate and the flame standoff distance are used to normalize the dual strand data. The single strand burning rate data of JA2 propellant were obtained by Kopicz et al.[1] The flame standoff distance is gathered from thermocouple traces reported by Kopicz at the specified

pressures. Figure 4.20 shows where the flame standoff distance is for each of the three pressures tested. The flame standoff is where the slope increases drastically.

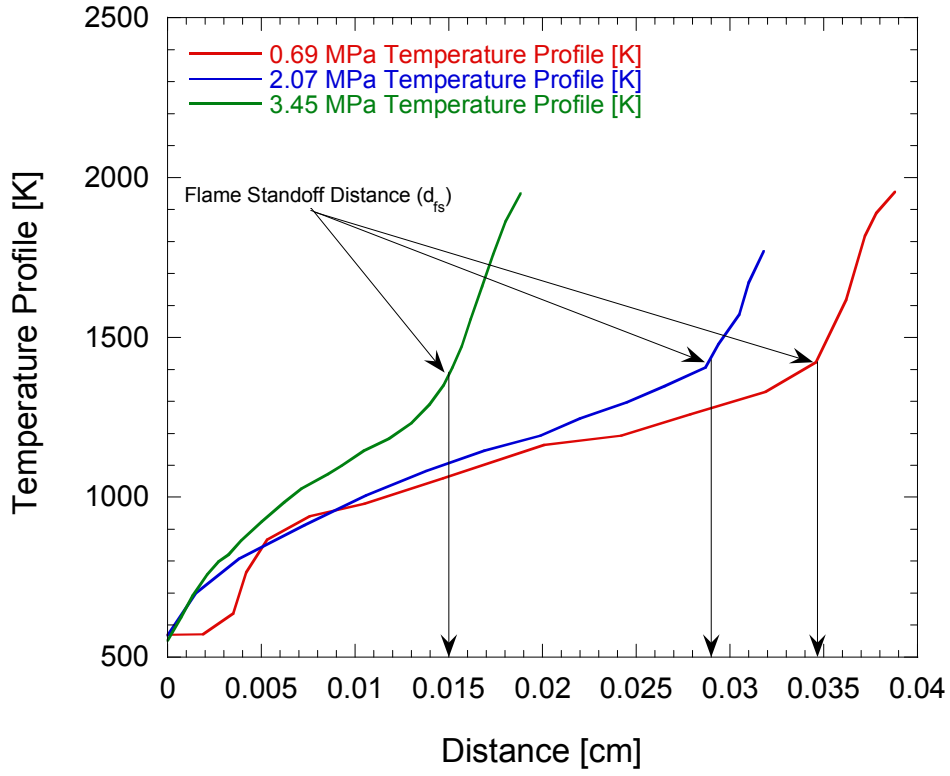

Figure 4.20 Thermocouple traces of JA2 propellant burning under steady-state conditions.

Figure 4.21 shows the plot of the dimensionless burning rate over the dimensionless gap distance. The dual strand burning rates are normalized by the single strand burning rate data, and the gap widths are normalized by the single strand flame standoff distance with pressure corrections. Using this method the three sets of data nearly collapse into one curve.

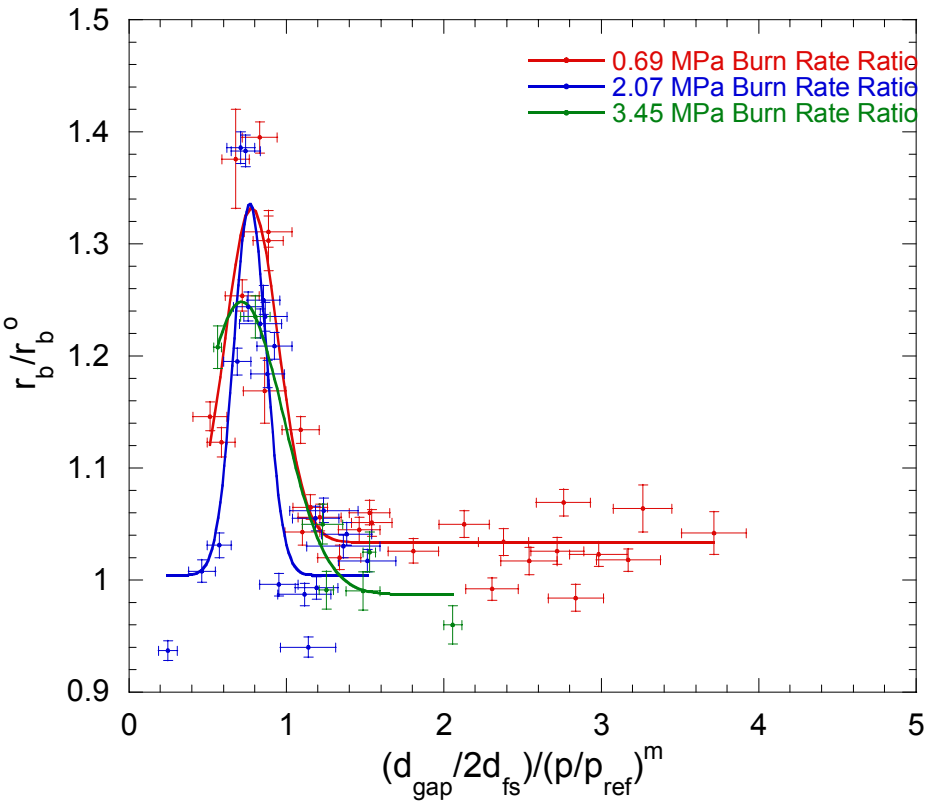

Figure 4.21 Normalized dual propellant strand burning data.

To obtain a mathematical form of the experimental data, two functions are considered: (1) a Gaussian function and (2) an inverse hyperbolic tangent function. The two functions are coupled together by a Heaviside function.[18] The Heaviside function outputs a zero or unity depending on the range.

$$H(x) \equiv \begin{cases} 0 & x < 0 \\ 1 & x > 0 \end{cases} \tag{4-1}$$

A modified Heaviside function with a step at x = 0.5 is

$$\mathrm{H}(\mathrm{x} - 0.5) = \begin{cases} 0 & \mathrm{x} < 0.5 \\ 1 & \mathrm{x} > 0.5 \end{cases} \tag{4-2}$$

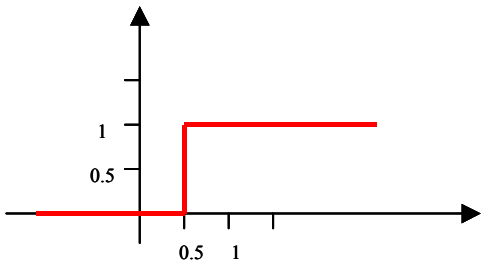

Figure 4.22 Heaviside function output for Equation (4-2).

This modified Heaviside function was used to serve as a multiplier to the Gaussian function in order to fit the data with dimensionless gap widths above 0.5. The difference of the two Heaviside functions, $D(x) \equiv H(x) - H(x-0.5)$, is used as a multiplier to the inverse hyperbolic tangent function in order to fit the data with dimensionless gap widths between 0 and 0.5.

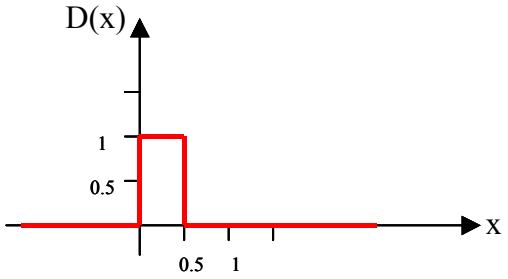

Figure 4.23 The difference of two Heaviside functions.

The following is the resulting equation that fits the data.

$$F(x) = A(x) + B(x) \tag{4-3}$$

$$A(x) = D(x)\left[0.43\tanh^{-1}(2x - 0.99) + 1.139\right] \tag{4-4}$$

$$B(x) = [H(x-0.5)]\left[1.01 + 0.35\exp\left[-0.5\left(\frac{x-0.75}{0.18}\right)^2\right]\right] \tag{4-5}$$

Figure 4.24 shows the Equation (4-3) fit to the normalized data. The curve fit is based upon the assumption that the burning rate of the propellant is zero at aero gap width. Using this equation with the know single strand burning parameters and chamber pressure, a prediction can be made as to what the burn rate of the JA2 propellant is at a given gap width.

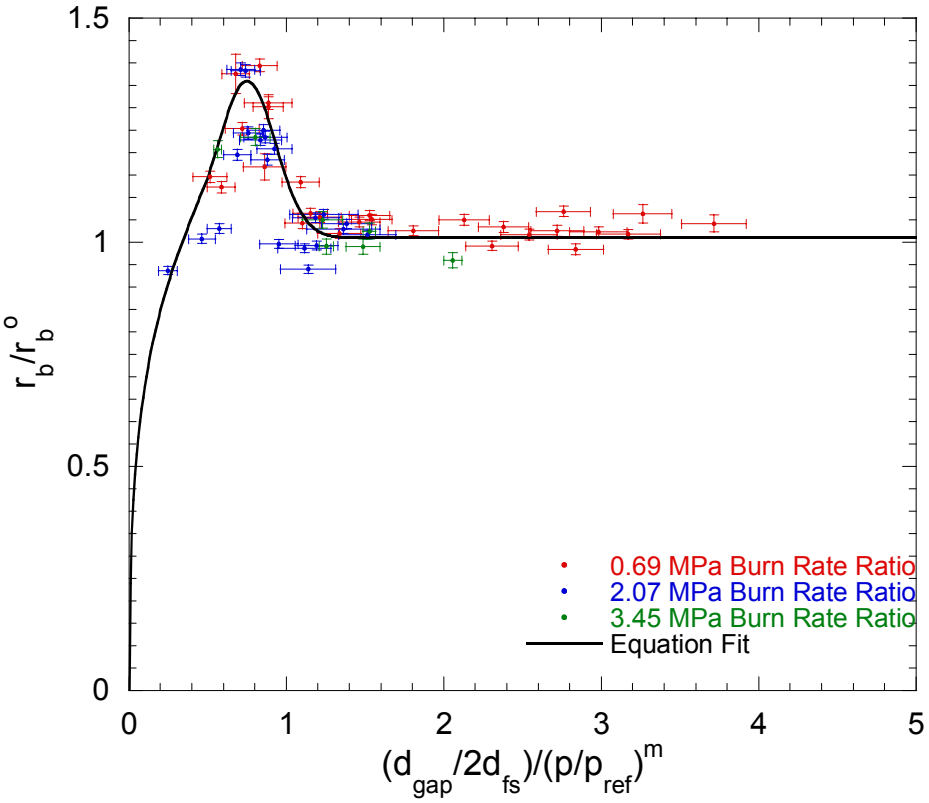

Figure 4.24 Comparison of curve-fit correlation to the normalized JA2 propellant burning rate data at different gap widths and pressures.

4.6 Burn Rate Observations

There are noticeable trends found at each pressure tested. At 0.69 MPa there is a substantial increase (about 40%) in the burning rate of dual strands at gap widths around 2.5 mm, compared to the burning rate of a single strand. As the gap width between strands is increased, the burning rate enhancement effect is dropped rapidly to an insignificant level.

At 2.07 MPa, the peak burning rate enhancement occurred at gap widths between 4 mm and 6 mm. The burning rate enhancement effect is still very strong (nearly 35% - 40%) in comparison with the burning rates of a single strand.

Even though only limited tests were conducted at 3.45 MPa, the general curve follows the same trend seen at 2.07 MPa testing. It seems to be shifted more towards smaller gap widths, so that the peak is at 4 mm. The peak also only shows a burning rate increase of 20%.

At all pressures tested, when the gap width is increased the burn rate for dual propellant strands approaches asymptotically to the burn rate of a single strand. When the gap width is large enough, the adjacent propellant flames do not affect each other, and the rate of energy feedback to the propellant burning surface is close to that of a single propellant strand burning case.

The merging or compression of the two propellant flames within the geometric confinement region is believed to be the main cause for burning rate enhancement. Essentially, the flame is closer to the burning surface, resulting in an increased rate of heat transfer. Thus, the burn rate is higher than that of the single strand. When the gap width is extremely small, the burn rate of the dual propellant strands can vary significantly depending upon the operating condition. It is anticipated that below a certain gap-width threshold the burn rate ratio will decrease as the gap width is further decreased. However, in this investigation the gap width could only be controlled above 1 mm. Below this level the JA2 burning surfaces are highly non-uniform, resulting in great difficulties for obtaining an accurate control of the gap width.

4.7 Error Analysis

The error analysis used for this investigation is a complicated process involving many steps. The error must be calculated for the measured gap width and the burning rate.

4.7.1 Time-Averaged Gap Width Error

Since the gap width is measured from a video screen there is error associated with the measured on-screen instantaneous gap widths at times t_1, (d_{m1}) and t_2, (d_{m2}), the actual specific diameter of the propellant sample, (d_p), the on-screen measured correction diameter, (d_c), the averaged on-screen gap width, (d_a), and the actual gap width, (d_{gap}). Any parameter measured from the video screen has an error coupled with the measuring scale and the finite resolution of the video screen. Therefore, the error of d_{m1}, d_{m2}, and d_c on the screen are on the order of 2 mm, i.e.,

$$\delta d_{m1} = \delta d_{m2} = \delta d_c = 2\,\text{mm} \tag{4-6}$$

The error associated with the actual specific diameter of the propellant sample is also a function of a measuring instrument. In this case the error takes into the account the error of the dial calipers used to measure the diameter of the propellant.

$$\delta d_p = .013\,\text{mm} \tag{4-7}$$

To find the time-averaged gap width Eq. (4-8) is used.

$$d_a = \frac{d_{m1} + d_{m2}}{2} \tag{4-8}$$

According to Taylor,[19] the error associated with the average gap width is the standard deviation of the mean since d_a is an average of d_{m1} and d_{m2}.

$$\delta d_a = \sigma_{\bar{x}} \tag{4-9}$$

where;

$$\sigma_{\bar{x}} = \frac{\sigma_x}{\sqrt{N}} \tag{4-10}$$

where N is the number of samples and σ_x is defined as

$$\sigma_x \equiv \sqrt{\frac{1}{N-1}\sum_{i=1}^{N} d_i^2} \tag{4-11}$$

$$\mathrm{d_i} = \mathrm{x_i} - \bar{\mathrm{x}} \tag{4-12}$$

$$\bar{\mathrm{x}} = \frac{\Sigma \mathrm{x_i}}{\mathrm{N}} \tag{4-13}$$

Finally, substituting Eqs. (4-10) to (4-13) into Eq. (4-9) yields

$$\delta d_a = \sqrt{\frac{\frac{1}{N-1}\left[\left[x_1 - \left[\frac{x_1+x_2}{N}\right]\right]^2 + \left[x_2 - \left[\frac{x_1+x_2}{N}\right]\right]^2\right]}{N}} \tag{4-14}$$

where; $x_1 = d_{m1}$, $x_2 = d_{m2}$, and N = 2.

Once the error associated with the on-screen measured time-averaged gap width is found, the error of d_{gap} can be found using the propagation of errors method seen in Eq. (4-15).[20]

$$\delta \mathrm{q} = \sqrt{\left(\frac{\partial \mathrm{q}}{\partial \mathrm{x_1}}\delta \mathrm{x_1}\right)^2 + \left(\frac{\partial \mathrm{q}}{\partial \mathrm{x_2}}\delta \mathrm{x_2}\right)^2 + \cdots + \left(\frac{\partial \mathrm{q}}{\partial \mathrm{x_n}}\delta \mathrm{x_n}\right)^2} \tag{4-15}$$

where q is a function of x_1 through x_n, i.e.,

$$\mathrm{q} = \mathrm{f}\left(\mathrm{x_1}, \mathrm{x_2}, \ldots, \mathrm{x_n}\right) \tag{4-16}$$

The value of d_{gap} is found by multiplying the averaged on-screen gap width, (d_a), by the actual specific diameter of the propellant sample, (d_p), divided by the on-screen measured correction diameter, (d_c), i.e.,

$$d_{gap} = \frac{d_p}{d_c} d_a \tag{4-17}$$

Taking the derivative with respect to each term yields Eqs. (4-18) to (4-20),

$$\frac{\partial d_{gap}}{\partial d_p} = \frac{d_a}{d_c} \tag{4-18}$$

$$\frac{\partial d_{gap}}{\partial d_a} = \frac{d_p}{d_c} \tag{4-19}$$

$$\frac{\partial d_{gap}}{\partial d_c} = -\frac{d_p d_a}{\left(d_c\right)^2} \tag{4-20}$$

Plugging Eqs. (4-18) to (4-20) back into Eq. (4-15),

$$\delta d_{gap} = \sqrt{\left(\frac{\partial d_{gap}}{\partial d_p}\delta d_p\right)^2 + \left(\frac{\partial d_{gap}}{\partial d_a}\delta d_a\right)^2 + \left(\frac{\partial d_{gap}}{\partial d_c}\delta d_c\right)^2} \tag{4-21}$$

$$\delta d_{gap} = \sqrt{\left(\frac{d_a \delta d_p}{d_c}\right)^2 + \left(\frac{d_p \delta d_a}{d_c}\right)^2 + \left(-\frac{d_p d_a \delta d_c}{\left(d_c\right)^2}\right)^2} \tag{4-22}$$

The error associated with the time-averaged gap width is computed for each test run.

4.7.2 Burn Rate Error

As previously stated the burn rate of the JA2 propellant is found by fitting a curve to the linear drive velocity data within the specified time range. This curve corresponds to the "least-squares fit method", and is given by the following equations,

$$y = A + Bx \tag{4-23}$$

$$A \equiv \frac{\sum_{i=1}^{N} x_i^2 \sum_{i=1}^{N} y_i - \sum_{i=1}^{N} x_i \sum_{i=1}^{N} x_i y_i}{\Delta} \tag{4-24}$$

$$B \equiv \frac{N \sum_{i=1}^{N} x_i y_i - \sum_{i=1}^{N} x_i \sum_{i=1}^{N} y_i}{\Delta} \tag{4-25}$$

$$\Delta \equiv \sum_{i=1}^{N} x_i^2 - \left(\sum_{i=1}^{N} x_i\right)^2 \tag{4-26}$$

Assuming the error in time is negligible compared to the error in distance, Eqs. (4-27) to (4-29) are used to calculate the error in y, A, and B.

$$\delta y = \sqrt{\frac{1}{N-1}\sum_{i-1}^{N}\left(y_i - A - Bx_i\right)^2} \tag{4-27}$$

$$\delta A = \delta y\sqrt{\frac{\sum_{i=1}^{N} x_i^2}{\Delta}} \tag{4-28}$$

$$\delta B = \delta y\sqrt{\frac{N}{\Delta}} \tag{4-29}$$

Seen from Eq. (4-23), B is the slope and is therefore the speed of the linear drive, and the error in the calculated regression rate is δB. Since there are two linear drives the burning rate is averaged from both sides given by Eq. (4-30).

$$r_b = \frac{r_{bL} + r_{bR}}{2} \tag{4-30}$$

This equation is in the same form as the equation for d_a, the error associated with r_b is the same as Eq. (4-14), where; $x_1 = r_{bL}$, $x_2 = r_{bR}$, and N = 2. The error associated with the burn rate is computed for each test run.

4.8 Experimental Setup Problem Observations

The low chamber pressures used for testing may seem to be too low in comparison with the actual pressures experienced during the ballistic cycle of a large caliber weapon system. However, the high loading density condition corresponds to the early stages of the ballistic cycle where the propellant strands are in close proximity. After the first few milliseconds the propellant will have burned back away from its neighboring propellants. Nevertheless, since the DWESB, can sustain pressures up to 31.03 MPa, higher chamber pressures were attempted. When the chamber pressure was raised to 5.17 and 6.89 MPa two main problems were encountered. Both of these problems can be attributed to the fact that at higher pressures, the burning rate of the propellant increases.

Firstly, significant amount of combustion product gases remained in the main combustion chamber for the camera to record a good image for the gap-width control. The increase in burning rate causes an increase in the rate of generation of combustion product gases. The DEWSB is unable to exhaust the product gases rapidly enough to allow the laser to pass through the combustion chamber. Therefore the image recorded is not clear enough for the control software to define distinct propellant surfaces.

Secondly, the linear ball screw binds at a higher feed rate. The increase in burning rate calls for an increase in the base- and high-feed rates supplied to the linear drive systems. When the baseline feed rate is set too high the linear ball screw binds up and there is no feeding. If the base is set low to accommodate this failure the propellant burns back too far before the high-speed feeding is activated.

As of now there has been no applicable solution to these problems presented. The ball screw may be able to be greased better to reduce the chance of it binding. However, efforts in reducing the amount of exhaust in the combustion chamber were already addressed and the feeling is that there is no possibility in increasing the exhaust flow out of the chamber more than what was already accomplished by adding the four new exhaust ports.

CHAPTER 5 Conclusions

1. At the pressure of 0.69 MPa a pronounced effect (~40 %) of gap width on burning rate of JA2 propellant was observed for a gap width of about 2.5 mm.
2. At the pressure of 2.07 MPa a pronounced effect (~35-40 %) of gap width on burning rate of JA2 propellant was observed for gap widths between 4 and 6 mm.
3. At the pressure of 3.45 MPa a pronounced effect (~20 %) of gap width on burning rate of JA2 propellant was observed for gap widths below 4 mm.
4. The burning rate of the dual strands reaches a peak level since the flame is forced to stay within the confined region.
5. For all pressures, when the gap width is large enough the dual strand burning rate reaches that of the single strand, since the propellant flame is no longer affected by the presence of adjacent flames.
6. The burning surfaces of the dual strands are non-flat due to sporadic carbonaceous residues being ejected from the surface generating highly luminous sites for radiation absorption, as well as the highly stretched flames with non-uniform flow distribution caused by radially out-flowing gases.

CHAPTER 6 Publications

6.1 Papers Published in Peer-Reviewed Journals

- N/A

6.2 Papers Published in Non-Peer-Reviewed Journals or Conference Proceedings

- Ferrara, P.J., Risha G.A., Boyer E., Bourdin C., and Kuo K.K., "Effect of Gap Width on Combustion Behavior of Two Opposing Propellant Surfaces," 39th AIAA/ASME/SAE/ASEE Joint Propulsion Conference and Exhibit, Huntsville, Alabama, July 20-23, 2003.
- Kenneth K. Kuo, Surajit Kumar, and Baoqi Zhang, "Transient Burning Characteristics Of JA2 Propellant Using Experimentally Determined Zel'dovich Map", 39th AIAA/ASME/SAE/ASEE Joint Propulsion Conference and Exhibit, Huntsville, Alabama, July 20-23, 2003.

6.3 Papers Presented at Meetings, but Published in Conference Proceedings

- N/A

6.4 Manuscripts Submitted, but Not Published

- Kenneth K. Kuo, Surajit Kumar, and Baoqi Zhang, "Transient Burning Characteristics Of JA2 Propellant Using Experimentally Determined Zel'dovich Map", Submitted to Journal of Propulsion and Power, March 31, 2003.
- Ferrara, P.J., Bourdin C., and Kuo K.K., "Simulation of Propellant Burning Behavior under High Loading Density Conditions by Studying the Combustion of Two Opposing Propellant Strands," Will be submitted to Journal of Propulsion and Power, August 2004.

6.5 Technical Reports Submitted to ARO

- Interim Progress Reports

CHAPTER 7 Participating Personnel

7.1 Principal Investigator

- Professor Kenneth K. Kuo

7.2 Obtained Doctoral Degree

- Grant A. Risha—worked partially on this project during his doctoral studies, at PSU

7.3 Obtained Masters Degree

- Peter J. Ferrara, MS degree conferred on 15 May 2004, at PSU
- Caroline Bourdin, participated as an exchange student at PSU, and used results from this project to satisfy her MS degree requirement for Engineering Internship from Ecole Nationale Supérieure de Méchanique et d' Aérotechnique, Poitiers-Futuroscope, Vienne (France), 30 August 2002
- Surajit Kumar, MS degree conferred on 15 December 2001, at PSU

7.4 Current Students

- Eric Boyer

7.5 Current Staff

- Professor Baoqi Zheng

CHAPTER 8 Inventions

N/A

REFERENCES

[1] Field, R.. and Kuo, K.K., "Observation of Multi-Dimensional Flame Structures of LOVA Propellants," 25th JANNAF Combustion Meeting, NASA Marshall Space Flight Center, Huntsville, AL, CPIA Publication 498, Vol. 2, pp. 127-134, October, 1988.

[2] Field, R.., "Observations of Surface Structure and Regression Behavior of Solid Propellant Strands Burning Under Narrow Gap Conditions," Doctorate Dissertation, The Pennsylvania State University, University Park, PA, 1993.

[3] Kuo, K.K., Gore, J. P., and Summerfield, M., "Transient Burning of Solid Propellants," Chapter 15 of Fundamentals of Solid-Propellant Combustion, Editors K. K. Kuo, and M. Summerfield, Progress in Astronautics and Aeronautics, AIAA Vol.90, pp. 599-660, 1984.

[4] Novozhilov, B.V., "Theory of Non-steady Burning and Combustion Stability of Solid Propellants by the Zeldovich-Novozhilov Method," Chapter 15 of Non-steady Burning and Combustion Stability of Solid propellants, Editors L. De Luca, E.W. Price, and M. Summerfield, Progress in Astronautics and Aeronautics, AIAA Vol.143, pp 601-641, 1990.

[5] Kuo, K. K. and Coates, G. R., "Review of Dynamic Burning of Solid Propellants in Gun and Rocket Propulsion Systems," Invited Lecture of 16th Symposium (International) on Combustion, Pittsburgh, PA, 1177-1191, 1976.

[6] Zel'dovich, Ya. B., Zhurnal Eksperimental noi o Theoretischeskoi Fiziki, Vol. 12, pp. 498-524,1942.

[7] Kopicz, C., Watson, T. J., Kuo, K. K., and Thynell, S. T., "Combustion Behavior and Thermochemical Properties of JA2 Propellant," *Challenges in Propellants and Combustion 100 Years After Nobel*, Begell House, Inc., New York, NY, pp. 559-573, 1997.

[8] Eisenreich, N., Weiser, V., Eckl, W., Fischer, T., Kelzenberg, S., Langer, G., "Phenomenon of The Combustion of The Gun Propellant JA2," *Combustion of Energetic Materials,* edited by K. K. Kuo and L. T. De Luca, Begell House, New York, pp. 251-262, 2000.

[9] Miller, M. S.,"Thermophysical Properties of Six Solid Gun Propellants," Army Research Laboratory report, Aberdeen Proving Ground, MD, March 1997.

[10] Watson, T. J., Kuo, K. K., and Thynell, S. T., "The Assessment of Dynamic Burning Behavior for JA2 Propellant Rods." 31st JANNAF Combustion Sub-Committee Meeting. . CPIA No. 620, Vol. 2, pp 247-258, October, 1994.

[11] Zenin, A. A., "Thermodynamics of Stable Combustion Waves of Solid Propellants,"Progress in Aeronautics and Astronautics, Vol. 143, pp.197-231, 1992.

[12] Kooker, D.E., and Nelson, C.W., "Numerical Solution of Solid Propellant Transient Combustion", *The Heat Transfer Division of the ASME*, 1977.

[13] Meyer, G. H., "Initial Value Methods for Boundary Value Problems (Theory and Application of Invariant Imbedding)", 100th Volume in the series Mathematics in Science and Engineering, editor R. Bellman, Academic Press, NY, 1973.

[14] Kubota, N., "Survey of Rocket Propellants and Their Combustion Characteristics." Chapter 1 of Fundamentals of Solid Propellants. AIAA Progress in Astronautics and Aeronautics, Vol. 90. Edited by Kuo, K.K., and Summerfield, M. 1984.

[15] Eisenreich, N., Eckl, W., Fischer, T., Weiser, V., Kelzenberg, S., and Langer, G., Baier, A., "Burning Phenomena of the Gun Propellant JA2," Propellants, Explosives, Pyrotechnics, Vol. 25, pp 143-148, 2000.

[16] Newport Optics Technical Reference, pp 572-575, 2003.

[17] Bray, K.N.C., "Premixed Turbulent Combustion in a Counterflow Geometry," Elsevier Science Publishers B.V., pp 355-374, 1993.

[18] Mathews, J., and Walker, R.L., *Mathematical Methods of Physics*, California Institute of Technology, California, pp 107-109, 1971.

[19] Taylor, J.R., *An Introduction to Error Analysis, 2nd Edition*, University Science Books, California, 1997.

[20] Risha, G. A., "Enhancement of Hybrid Rocket Combustion Performance Using Nano-Sized Energetic Particles," Doctorate Dissertation, The Pennsylvania State University, pp274-278, 2003.

APPENDIX A LabVIEW Code

The following figures are of the LabVIEW code used to control the gap width real time during a test.

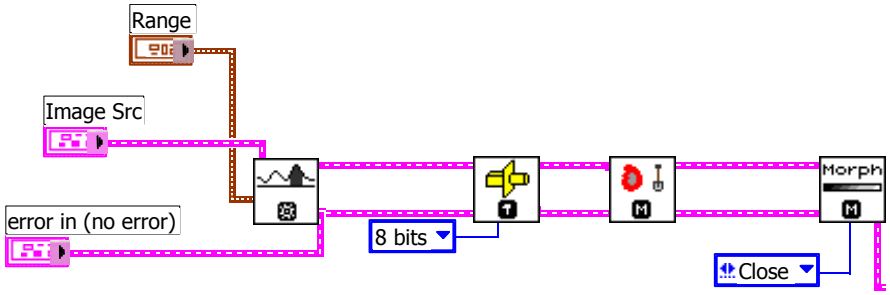

Figure A.1 Image processing.

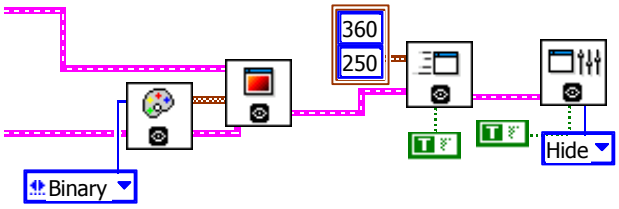

Figure A.2 Image display.

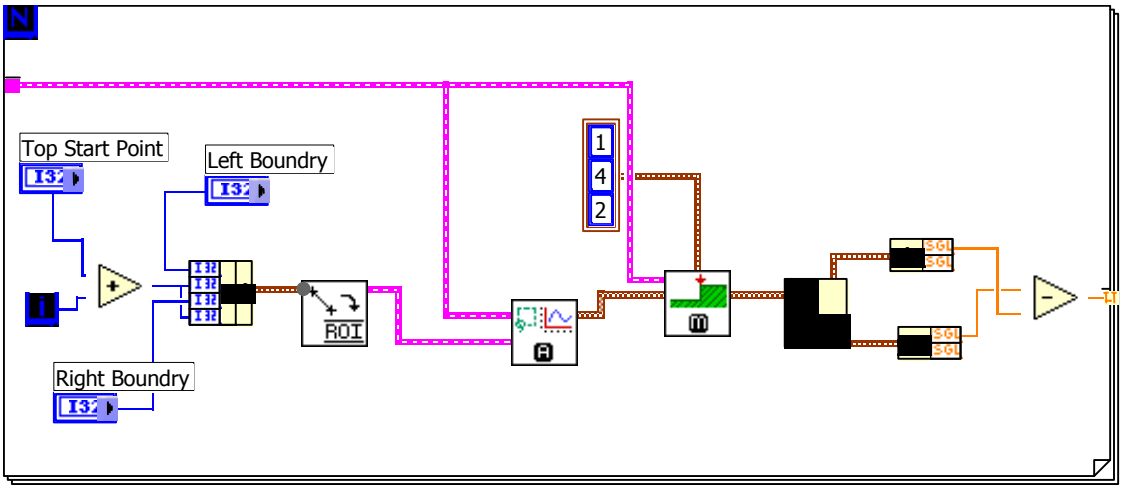

Figure A.3 Gap width measuring code.

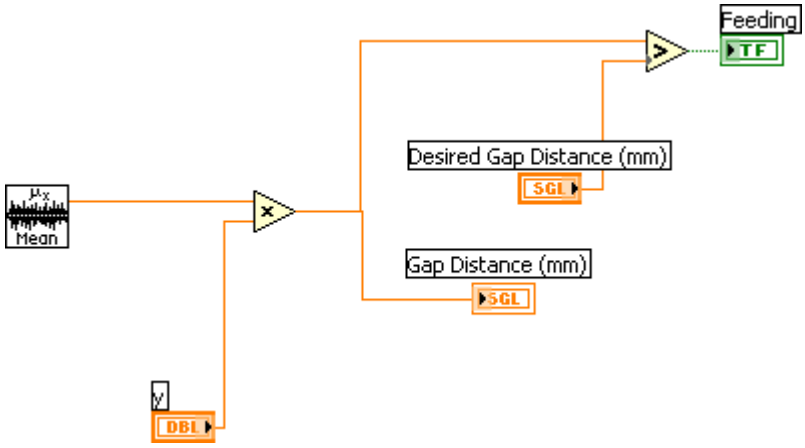

Figure A.4 Measured gap width and user specified gap width comparison loop.

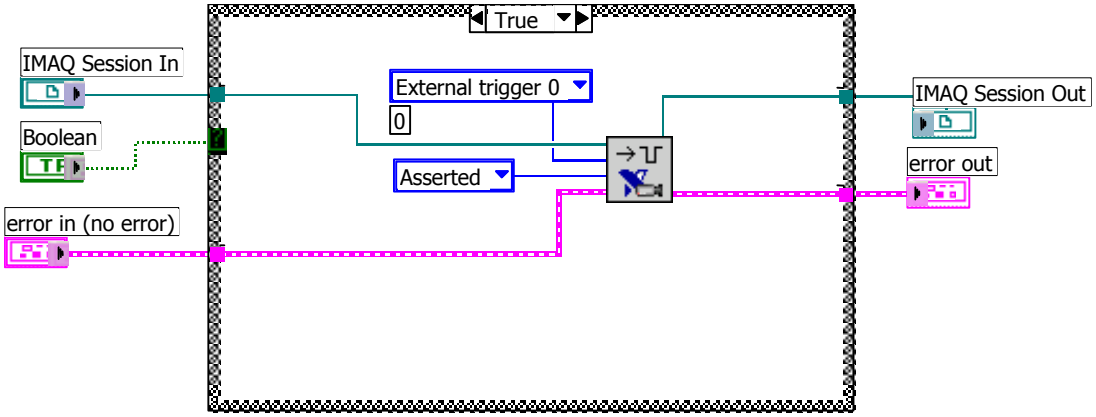

Figure A.5 High-speed control trigger.